# 11

# Vortical Aerodynamic Force and Moment

## 11.1 Introduction

As an applied branch of fluid dynamics, aerodynamics (and hydrodynamics) studies the force and moment experienced by solid bodies moving through the fluid. In order to fully understand relevant mechanisms, aerodynamics has a task in common to general fluid dynamics: investigating various flow phenomena generated by the body motion. In addition, the ultimate concern of aerodynamics, also its unique task, is *expressing the force and moment in a way that can precisely capture the key physical mechanisms contributing to these integrated performances.*

*Low-speed aerodynamics* is dominated by the shearing process, of which the necessary physical knowledge has been discussed in preceding chapters. Therefore, it is natural now to further identify those specific key shearing processes that contribute most significantly to the force and moment for any given body motion at low Mach numbers. This task requires developing some special theories. We focus on incompressible flow, but some theories also cover compressible flow. It can then be seen that, as the Mach number increases, the compressing process is progressively important for the force and moment and becomes dominant in supersonic flow.

The main concern of this chapter is a basic external-flow problem: a material body of volume $B$ moves arbitrarily in a viscous fluid. The body may have arbitrarily deformable boundary, as encountered in several areas such as fish swimming and insect flight in external biofluiddynamics, nonlinear fluid–solid coupling, and flow control by flexible walls, etc.[1] Thus, we assume the body surface $\partial B$ has specified velocity distribution $\boldsymbol{u} = \boldsymbol{b}(\boldsymbol{x}, t)$. The fluid volume $V_\mathrm{f}$ is bounded internally by the material surface $\partial B$ and externally by a control surface $\Sigma$. The latter may have arbitrary velocity $\boldsymbol{v}(\boldsymbol{x}, t)$ or extend to infinity where the fluid is at rest or in uniform translation. The flow domain is sketched in Fig. 11.1.

[1] Some of the theories can also be applied to gas–liquid two-phase flow by adding the surface tension effect.

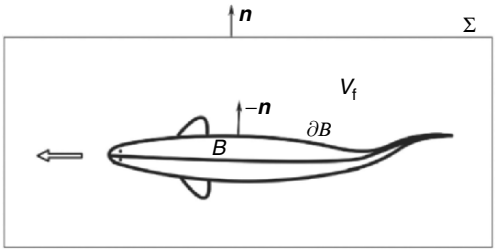


**Fig. 11.1.** Flow domain to be analyzed and notations

### 11.1.1 The Need for "Nonstandard" Theories

The general expressions of aerodynamic force and moment are *"standard"* formulas (2.71) and (2.72). For an incompressible external flow defined in Fig. 11.1, by the Reynolds transport theorem (2.37), these formulas take the following alternative forms, based on (a) direct integrals of surface stresses and their moments over $\partial B$, (b) integrals of local balance of momentum and angular momentum, and (c) the rate of change of total momentum and angular momentum in a generic control volume:

$$\boldsymbol{F} = -\int_{\partial B} (-p\boldsymbol{n} + \boldsymbol{\tau})\,\mathrm{d}S \tag{11.1a}$$

$$= -\rho \int_{V_f} \boldsymbol{a}\,\mathrm{d}V + \int_{\Sigma} (-p\boldsymbol{n} + \boldsymbol{\tau})\,\mathrm{d}S \tag{11.1b}$$

$$= -\rho \frac{\mathrm{d}}{\mathrm{d}t} \int_{V_f} \boldsymbol{u}\,\mathrm{d}V + \int_{\Sigma} [-p\boldsymbol{n} + \boldsymbol{\tau} - \rho\boldsymbol{u}(u_n - v_n)]\,\mathrm{d}S, \tag{11.1c}$$

$$\boldsymbol{M} = -\int_{\partial B} \boldsymbol{x} \times (-p\boldsymbol{n} + \boldsymbol{\tau})\,\mathrm{d}S + \boldsymbol{M}_{\mathrm{s}B} \tag{11.2a}$$

$$= -\rho \int_{V_\mathrm{f}} \boldsymbol{x} \times \boldsymbol{a}\,\mathrm{d}V + \int_{\Sigma} \boldsymbol{x} \times (-p\boldsymbol{n} + \boldsymbol{\tau})\,\mathrm{d}S + \boldsymbol{M}_{\mathrm{s}\Sigma} \tag{11.2b}$$

$$= -\rho \frac{\mathrm{d}}{\mathrm{d}t} \int_{V_\mathrm{f}} \boldsymbol{x} \times \boldsymbol{u}\,\mathrm{d}V + \int_{\Sigma} \boldsymbol{x} \times [-p\boldsymbol{n} + \boldsymbol{\tau} - \rho\boldsymbol{u}(u_n - v_n)]\,\mathrm{d}S + \boldsymbol{M}_{\mathrm{s}\Sigma}. \tag{11.2c}$$

Here, $\boldsymbol{a} = \mathrm{D}\boldsymbol{u}/\mathrm{D}t$ is the fluid acceleration and we have used the triple decomposition of the stress $\boldsymbol{t} = -p\boldsymbol{n} + \boldsymbol{\tau} + \boldsymbol{t}_\mathrm{s}$, with $\boldsymbol{\tau} = \mu\boldsymbol{\omega} \times \boldsymbol{n}$ and $\boldsymbol{t}_\mathrm{s}$ being the shear stress and the stress due to surface deformation, respectively, see (2.149) and (2.150). We have bypassed the need for calculating the local $\boldsymbol{t}_\mathrm{s}$ (which may

be complicated on a deformable surface) as much as possible. The effect of $\boldsymbol{t}_\mathrm{s}$ vanishes in (11.1), while that of $\boldsymbol{x} \times \boldsymbol{t}_\mathrm{s}$ in (11.2) has been integrated out, see (2.153):

$$\boldsymbol{M}_{\mathrm{s}B} = -2\mu \int_{\partial B} \widehat{\boldsymbol{n}} \times \boldsymbol{b} \, \mathrm{d}S = -2\mu \int_B \boldsymbol{\omega}_B \, \mathrm{d}V, \tag{11.3a}$$

$$\boldsymbol{M}_{\mathrm{s}\Sigma} = -2\mu \int_\Sigma \boldsymbol{n} \times \boldsymbol{u} \, \mathrm{d}S = -2\mu \int_V \boldsymbol{\omega} \, \mathrm{d}V, \tag{11.3b}$$

where $\widehat{\boldsymbol{n}} = -\boldsymbol{n}$ is the outward normal of $\partial B$ and $V = V_\mathrm{f} + B$. The total vorticity in $B$ or $V$ can evidently be expressed by the total circulation in two dimensions and by (3.14) in three dimensions. Of these alternative formulas, forms (b) and (c) will be identical if $V_\mathrm{f}$ is a material fluid volume. Form (a) is most primary but may also be viewed as the special case of (b) or (c): If $\Sigma$ shrinks to the body surface $\partial B$ so that $V_\mathrm{f} = 0$, then since the direction of $\boldsymbol{n}$ on $\Sigma$ is opposite to that on $\partial B$, (b) or (c) is reduced to (a).

These formulas, however, are not physically most revealing. What appear in their integrand are variables like velocity, pressure, and density themselves, but the mechanisms leading to their specific distribution in a flow field and at the body surface are hidden. These mechanisms come from *local dynamics* governed by

$$\rho \boldsymbol{a} = -\nabla p + \mu \nabla^2 \boldsymbol{u} = -\nabla p - \mu \nabla \times \boldsymbol{\omega}, \tag{11.4}$$

$$\nabla \times \boldsymbol{a} = \frac{\partial \boldsymbol{\omega}}{\partial t} + \nabla \times (\boldsymbol{\omega} \times \boldsymbol{u}) = \nu \nabla^2 \boldsymbol{\omega}, \quad \nu = \mu/\rho, \tag{11.5}$$

where one sees the *spatial and temporal derivatives* of the relevant variables. It is the interactions of these derivatives that form various flow structures which at large Reynolds numbers are highly localized but may dominate the integrated performance. Thus, there is a theoretical gap between standard formulas and local dynamics. This gap cannot be eliminated by simply substituting (11.4) into (11.1b) and (11.2b), because the pressure $p$ is a global effect of all interactions; it is actually the quantity that one wishes most to remove or replace by other local dynamic processes.

For example, at large Reynolds numbers, by (11.1a) we know that the lift on an airfoil is dominated by the pressure difference on its both surfaces, which is in turn explainable by the Bernoulli equation due to a larger fluid speed on the upper surface. But a deeper physical question is: Why the fluid runs faster on the upper surface?

A popular heuristic answer to this question is: The fluid particles that separate at the front stagnation point have to meet again at the trailing edge. This story is, however, wrong. The timelines (Sect. 2.1) in Fig. 11.2 indicate that the fluid on the upper surface runs even faster than needed for meeting the fluid from the lower surface at the trailing edge. No explanation can be directly found from (11.1).

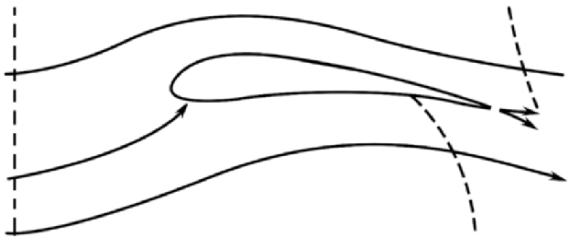

**Fig. 11.2.** Potential flow over a Joukowski airfoil. *Dashed lines* are time lines. Reproduced from Panton (1984)

More generally, the above theoretical gap exists between any integrated performances and their key local contributors. It makes the physical understanding, flow diagnosis, and configuration design lose the most valuable guidance. The awareness of this gap is becoming clearer as one's strong pursuit of carefully and optimally designed high-performance configurations. Suppose one is given a set of finite-domain data for a viscous flow over a body. One can then calculate the stress on the wall and apply (11.1a) to get the force. Then one may look at various fields in the domain: streamlines, velocity vectors, the contours of pressure and vorticity, etc. These together form a quite complete physical picture of the flow. However, if one wishes to identify the physical mechanisms that result in that force status, only some qualitative assessments can be drawn from these plots. They are still insufficient to pinpoint what flow structures have net contribution to the force, in what way, how, and why.

### 11.1.2 The Legacy of Pioneering Aerodynamicist

In fact, filling the aforementioned gap has been a long-term effort in the development of aerodynamics, where the "standard" formulas are only a starting point rather than the final form of the theory. Instead, a great milestone in the development of classic aerodynamics is the well-known *circulation theory*, where the aerodynamic force is expressed by elegant "*nonstandard*" formulas in terms of the circulation $\Gamma$ of a wing section. The historical significance of the circulation theory has been well described by Wu (2005):

*"The task of finding theoretical solutions to practical aerodynamic flow problems was (and still is) formidably difficult. Bypassing flow details as much as possible was indeed the only strategy open to the pioneering aerodynamicist. Together with simplifications of the inviscid-fluid assumption, this strategy served as the springboard for the dazzling developments of aerodynamics a century ago by leading scholars in Europe: Kutta, Joukouski, Lanchester, Prandtl, among others."*

To see how this strategy worked so successfully, let us briefly recall the circulation theory for steady flow. This includes the Kutta–Joukowski formula (see Joukowski 1931)

$$L = -\rho U \Gamma \tag{11.6}$$

for the lift of a two-dimensional airfoil, and Prandtl's *lifting-line theory* for the lift and *induced drag* of a three-dimensional wing (e.g., Prandtl and Tietjens 1934; Glauert 1947)[2]:

$$L \simeq \rho U \int_{-s}^{s} \Gamma(y)\,\mathrm{d}y, \tag{11.7a}$$

$$D_{\mathrm{in}} \simeq -\rho \int_{-s}^{s} w(y)\Gamma(y)\,\mathrm{d}y, \tag{11.7b}$$

where $s$ is the semi-span and

$$w(y) = -\frac{1}{4\pi}\int_{-s}^{s} \frac{\mathrm{d}\Gamma(y')}{\mathrm{d}y'}\frac{\mathrm{d}y'}{y-y'} < 0 \tag{11.8}$$

is the *downwash velocity* (usually estimated at the 1/4-chord point, i.e., the aerodynamic center). Both theories are valid for streamlined wings in the limit of $Re \to \infty$. Note that $\Gamma$ does not appear in (11.1) at all; but it is this quantity that immediately reveals that the physical root of the force and moment is the vorticity in wing boundary layers and vortical wake formed thereby. In particular, the key to arriving at (11.7) was the ingenious insight of Prandtl and Lanchester that, owing to Helmholtz's vorticity theorems and in linearized approximation, a finite-span wing produces a *horseshoe vortex system* consisting of a bound line vortex (the *lifting line*) along the 1/4-chord line of the wing and a flat wake vortex sheet with variable strength[3]

$$\boldsymbol{\gamma}(y) = \boldsymbol{e}_x \gamma(y) = -\boldsymbol{e}_x \frac{\mathrm{d}\Gamma}{\mathrm{d}y}, \tag{11.9}$$

Fig. 11.3.[4] Then, (11.8) is merely a simple application of the Biot–Savart formula (3.31) to the horseshoe vortex system.

Evidently, the circulation theory has indeed bypassed the flow details as much as possible, narrowing the unknowns down to a single circulation $\Gamma$ to be solved for calculating the forces. In two dimensions, it is obtainable by using complex variable and conformal mapping (e.g., Lighthill 1986b). On the flow plane $z = x + \mathrm{i}y = r\mathrm{e}^{\mathrm{i}\varphi}$ there exists analytical complex velocity potential $w(z) = \phi + \mathrm{i}\psi$, and one maps the airfoil onto $a$ unit circle $\zeta = \mathrm{e}^{\mathrm{i}\theta}$ on the

[2] For two-dimensional flows we work on the $(x, y)$-plane, so that a clockwise circulation is negative as in the case around an airfoil with positive lift. But for three-dimensional flows we follow the convention that, in a *wind-axis system*, $(x, y, z)$ are along the oncoming flow, wing-span, and vertical up directions, respectively, see Fig. 7.18. Thus on an $(x, z)$-plane a clockwise circulation is positive.

[3] In linear approximation the rolling-up of vortex sheet due to self-induction, see Sects. 4.4.4 and 7.3, is entirely ignored.

[4] Ideally, the horseshoe vortex system becomes closed loop by the starting vortex at downstream infinity that retreats continuously with velocity $U$.

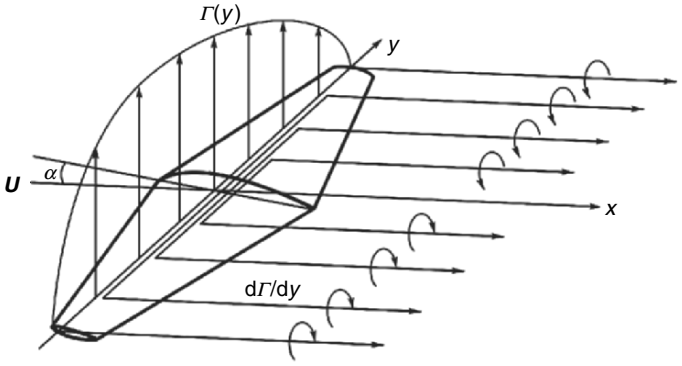


**Fig. 11.3.** The steady horseshoe vortex system of a thin wing

$\zeta$ plane. In that plane one considers the flow $U\mathrm{e}^{\mathrm{i}\alpha}$ over the circle at incidence $\alpha$ with *arbitrary* circulation $\Gamma$:

$$\frac{\mathrm{d}w}{\mathrm{d}\zeta} = u - \mathrm{i}v = U\left(\mathrm{e}^{-\mathrm{i}\alpha} - \frac{\mathrm{e}^{\mathrm{i}\alpha}}{\zeta^2}\right) + \frac{\Gamma}{2\pi\mathrm{i}\zeta},$$

which yields

$$\frac{\mathrm{d}w}{\mathrm{d}\zeta} = -\mathrm{i}\mathrm{e}^{-\mathrm{i}\theta}\left[2U\sin(\alpha-\theta) + \frac{\Gamma}{2\pi}\right] \quad \text{at} \quad \zeta = \mathrm{e}^{\mathrm{i}\theta}.$$

The trailing edge of the airfoil can always be managed to map to $\zeta = 1$, thus the Kutta condition (Sect. 4.4.2) requires $\mathrm{d}w/\mathrm{d}\zeta = 0$ at $\theta = 0$. This gives $\Gamma = -4\pi U \sin\alpha$, so by (11.6) the lift coefficient is

$$C_l = \frac{L}{\frac{1}{2}\rho U^2 c} = \frac{8\pi}{c}\sin\alpha, \tag{11.10}$$

where the chord length $c$ of the airfoil depends on the specific mapping function and equals 4 for a flat plate, which is almost true for any thin airfoil as well. This leads to the well-known simple formula

$$C_l = 2\pi\sin\alpha \simeq 2\pi\alpha \quad \text{for} \quad \alpha \ll 1. \tag{11.11}$$

Then, for a large-span wing, (11.6) holds approximately at every wing section, so $\Gamma(y)$ in (11.7) is known. However, the relative downwash $w/U$ implies a reduction of the effective angle of attack that reduces the circulation and causes the induced drag (11.7b). This observation leads to an integral equation

$$\Gamma(y) = \pi U c(y)\left[\alpha(y) - \frac{1}{4\pi U}\int_{-s}^{s}\frac{\mathrm{d}\Gamma(y')}{\mathrm{d}y'}\frac{\mathrm{d}y'}{y-y'}\right], \quad \alpha \ll 1, \tag{11.12}$$

of which the solution can be obtained analytically (e.g., Glauert 1947; Anderson 1991), with the famous conclusion that *a wing with elliptical load distri-*

*bution has minimum induced-drag.* Note that, remarkably, in the above entire two- and three-dimensional circulation theory one only needs to find the mapping function $\zeta = f(z)$; no flow field needs to be solved at all.

Now, modern aerodynamics is facing many new challenging problems, in which the flow complexity is far beyond the reach of any analytical solutions. Meanwhile, advanced experimental and numerical techniques have made it possible, at least in principle, to obtain detailed and complete data bases for such complex flows. Thus, the force $\boldsymbol{F}$ and moment $\boldsymbol{M}$ may follow at once by substituting the data into (11.1) and (11.2) or their compressible version. This being the case, then, is there still any need for "nonstandard" formulas as those pioneers did to explicitly reveal the key physical mechanisms responsible $\boldsymbol{F}$ and $\boldsymbol{M}$?

The answer is positive. Modern aerodynamics is not merely a simple combination of the flow data and standard formulas like (11.1) and (11.2). The more complicated the flow is, the more important role will the key physical factors play. "Bypassing flow details as much as possible" so as to reveal the key physical factors to $\boldsymbol{F}$ and $\boldsymbol{M}$ is actually the most valuable legacy of the pioneering aerodynamicists, which should be continued and further enriched. Modern versions of the "nonstandard" formulas are still highly desired, but their integrand can now be obtained experimentally or numerically rather than necessarily by approximate theories. Namely, the formulas should be exact and general. They can serve not only as a basis for deducing various approximate theories (including the circulation theory) but also as a powerful tool in flow analysis, diagnosis, and optimal configuration design.

### 11.1.3 Exact Integral Theories with Local Dynamics

In order to bridge the theoretical gap between integral performance and local dynamics, we need systematic approaches able to transform standard integral formulas to nonstandard forms, so that the local dynamic processes that have crucial *net* contribution to the force and moment can stand out explicitly. Currently, there are two types of theories that fit this need, to which this entire chapter is devoted.

One type is the *projection theory* to be presented in Sect. 11.2, which projects each term of the Navier–Stoke equation onto a vector space spanned by properly chosen harmonic vectors. The force and moment due to nonlocal pressure effect is replaced by other quantities describing local shearing and compressing processes. The theory has been formulated for externally unbounded flow problems.

Another type of theories with wider versatility is based on various *derivative moment transformations* (DMT for short), which execute multidimensional integration by parts to cast the original integrand to a moment of its derivatives (see Appendix A.2), and of which we have seen a few kinematic examples in Chap. 3. Of this type of DMT-based force and moment theories, there first appeared the *vorticity moment theory*, which expresses the

total force and moment by the rate of change of vortical impulse and angular impulse (the first- and second-order vorticity moments, respectively) introduced in Sect. 3.4.1. The theory is valid for incompressible flow and contains classic results like (11.6) and (11.7) as its direct corollaries. Then, after this theory there appeared the *boundary vorticity-flux theory*, which expresses the total force and moment in terms of the first and second moments of the stress-related boundary vorticity fluxes introduced in Sect. 4.1.3. The theory may cover viscous compressible flow over any deformable closed or open solid surface or fluid interface, and has been applied to innovative aerodynamic diagnosis and configuration design in both external and internal flow problems. Actually, the boundary vorticity-flux theory is a special case of a more general DMT-based theory for an arbitrary domain, whose consistency with the vorticity moment theory can also be easily verified.

DMT-based theories will be presented in Sects. 11.3–11.5. Typical applications of the projection theory and DMT-based theories in theoretical development and flow diagnosis will be exemplified, and their linkage to classic aerodynamics will be addressed. Whenever possible, we shall also point out how to extend the theory to compressible flow with constant or variable $\mu$ governed by (2.134) or (2.160), respectively. Here we just mention that the vortical form of (2.134) is[5]

$$\rho \boldsymbol{u}_{,t} + \rho \boldsymbol{\omega} \times \boldsymbol{u} - \frac{1}{2} q^2 \nabla \rho = -\nabla \Pi_0 - \nabla \times (\mu \boldsymbol{\omega}), \quad \Pi_0 = \Pi + \frac{1}{2} \rho q^2. \quad (11.13)$$

## 11.2 Projection Theory

Consider a set of basis vectors $\nabla \psi_i$ satisfying $\nabla^2 \psi_i = 0$, $i = 1, ..., n$, $n = 2, 3$. Take the inner product of (11.13) and $\nabla \psi_i$, and integrate the result over $V_\mathrm{f}$. By using identities

$$\nabla \psi_i \cdot \nabla \beta = \nabla \cdot (\beta \nabla \psi_i), \quad \nabla \psi_i \cdot (\nabla \times \boldsymbol{A}) = \nabla \cdot (\boldsymbol{A} \times \nabla \psi_i)$$

for any scalars $\beta$ and vector $\boldsymbol{A}$, we obtain $n$ scalar equations

$$\int_{V_\mathrm{f}} \left( \rho \frac{\partial \boldsymbol{u}}{\partial t} + \rho \boldsymbol{l} - \frac{1}{2} q^2 \nabla \rho \right) \cdot \nabla \psi_i \, \mathrm{d}V = \int_{\partial B} (-\Pi_0 \boldsymbol{n} + \boldsymbol{\tau}) \cdot \nabla \psi_i \, \mathrm{d}S - \int_{\Sigma} \Pi_0 \boldsymbol{n} \cdot \nabla \psi_i \, \mathrm{d}S, \quad (11.14)$$

where $\boldsymbol{l} \equiv \boldsymbol{\omega} \times \boldsymbol{u}$ is the Lamb vector. The control surface $\Sigma$ is assumed fixed and sufficiently large with $\boldsymbol{\omega} = \boldsymbol{0}$ thereon. In (11.14) each term is a weighted integral of a constituent of inertial or surface force. Depending on the specific choice of $\psi_i$, two versions of the theory have been developed. We focus on the total force; the total moment can be similarly treated by a different set of basis vectors as will be briefly mentioned.

[5] Unlike the analysis of vorticity evolution and interaction, in considering the force and moment the equations for momentum and angular momentum have to be expressed in terms of per unit volume.

### 11.2.1 General Formulation

The primary goal of the projection theory is to re-express the integrated pressure force over $\partial B$ by the integrations of vorticity and density gradient. The approach was first introduced by Quartapelle and Napolitano (1983) for viscous incompressible flow. For compressible flow considered by Chang and Lei (1996a), we replace the total pressure force by that due to normal stress $\varPi$, denoted by $\boldsymbol{F}_{\varPi}$. Its difference from $\boldsymbol{F}_{\mathrm{p}}$ is small at large Reynolds numbers.

An inspection of (11.14) indicates that to construct the $i$th component of $\boldsymbol{F}_{\varPi}$ we simply need $\boldsymbol{n}\cdot\nabla\psi_i = \boldsymbol{n}\cdot\boldsymbol{e}_i$ on $\partial B$, where $\boldsymbol{e}_i$ is the unit vector along the $i$th Cartesian coordinate, since then $-\varPi_0\boldsymbol{n}\cdot\nabla\psi_i = -\varPi_0 n_i$. To remove the integral over $\varSigma$ or make it able to be explicitly estimated, we need $\boldsymbol{n}\cdot\nabla\psi_i$ to vanish at infinity. This pair of boundary conditions for $\psi_i$ is nothing but (2.185) for the potential $\widehat{\phi}_i$ caused by the body motion with unit velocity $\boldsymbol{U} = -\boldsymbol{e}_i$. By (2.174), $\nabla\widehat{\phi}_i$ decays as $O(|\boldsymbol{x}|^{-n})$ as $|\boldsymbol{x}|\to\infty$. More precisely, when the body moves with constant velocity, let $\varSigma$ be a big sphere of radius $|\boldsymbol{x}| = x = R$, then the boundary integral is negligible if (Chang and Lei 1996a)

$$\frac{1}{R}\max_{x=R}(|\varPi|, \rho q^2, |\boldsymbol{t}_{\mathrm{vis}}|)\to 0 \quad \text{uniformly as} \quad R\to\infty. \tag{11.15}$$

Chang et al. (1998) demonstrate that this condition imposes no strict limitation to flows of practical interest. When the body has acceleration, somecontribution from $\varSigma$ will appear due to compressibility(Chang and Lei 1996a). Thus, for a nonaccelerating body, from (11.14) and (2.185) it follows that

$$F_{\varPi i} = -\int_{V_{\mathrm{f}}}\left(\rho\frac{\partial\boldsymbol{u}}{\partial t} + \rho\boldsymbol{l} - \frac{1}{2}q^2\nabla\rho\right)\cdot\nabla\widehat{\phi}_i\,\mathrm{d}V + \int_{\partial B}\boldsymbol{\tau}\cdot\nabla\widehat{\phi}_i\,\mathrm{d}S. \tag{11.16}$$

Now the integral of $\boldsymbol{u}_{,t}$ is well convergent. This effect can be further localized in incompressible flow (Howe 1995). For example, for a linearly accelerating body with velocity $\boldsymbol{U}(t)$, since

$$\int_{V_{\mathrm{f}}}\boldsymbol{u}_{,t}\cdot\nabla\widehat{\phi}_i\,\mathrm{d}V = \int_{\partial B}\boldsymbol{u}_{,t}\cdot\boldsymbol{n}\widehat{\phi}_i\,\mathrm{d}S = \dot{U}_j\int_{\partial B}n_j\widehat{\phi}_i\,\mathrm{d}S,$$

the first term of (11.16) can be written in terms of the *virtual mass tensor* defined by (2.186). Thus the total force due to pressure reads

$$F_{\mathrm{p}i} = -M_{ij}\dot{U}_j - \rho\int_{V_{\mathrm{f}}}(\boldsymbol{\omega}\times\boldsymbol{u})\cdot\nabla\widehat{\phi}_i\,\mathrm{d}V + \int_{\partial B}(\mu\boldsymbol{\omega}\times\boldsymbol{n})\cdot\nabla\widehat{\phi}_i\,\mathrm{d}S.$$

Moreover, set $\boldsymbol{u} = \boldsymbol{U} + \boldsymbol{v}$ such that $\boldsymbol{v}$ is the relative velocity (the velocity viewed in the frame fixed to the body), since

$$\begin{aligned}(\boldsymbol{\omega}\times\boldsymbol{U})\cdot\nabla\widehat{\phi}_i &= \widehat{\phi}_{i,k}(U_j u_{k,j} - u_{j,k}U_j) = u_{k,j}(U_j\widehat{\phi}_{i,k} - U_k\widehat{\phi}_{i,j})\\ &= [U_j u_k\widehat{\phi}_{i,k} - U_k u_j\widehat{\phi}_{i,k} - U_k u_k\widehat{\phi}_{i,j}]_{,j},\end{aligned}$$

the volume integral of $(\boldsymbol{\omega}\times\boldsymbol{U})\cdot\nabla\widehat{\phi}_i$ can be cast to surface integral over $\partial B$ with $\boldsymbol{u}=\boldsymbol{U}$ thereon. Thus, what left is an integral of $\boldsymbol{n}\cdot\nabla\widehat{\phi}_i\,\mathrm{d}S=n_i\,\mathrm{d}S$ by (2.185a), which, however, vanishes on closed surface. Therefore, we have

$$F_{\mathrm{p}i}=-M_{ij}\dot{U}_j-\rho\int_{V_{\mathrm{f}}}(\boldsymbol{\omega}\times\boldsymbol{v})\cdot\nabla\widehat{\phi}_i\,\mathrm{d}V+\int_{\partial B}(\mu\boldsymbol{\omega}\times\boldsymbol{n})\cdot\nabla\widehat{\phi}_i\,\mathrm{d}S, \quad (11.17)$$

indicating that the contribution from the Lamb vector comes from the flow region away from $\partial B$. Equation (11.17) decomposes $\boldsymbol{F}_{\mathrm{p}}$ into a virtual mass effect, an inviscid Lamb-vector integral, and a viscous surface-vorticity integral. Note that, however, in real viscous fluid the acyclic potential flow and its associated virtual-mass effect must cause a vortex sheet $\boldsymbol{\gamma}_{\mathrm{ac}}$, which holds exactly in the asymptotic limit of $\nu\to 0$ but is only an approximation at finite Reynolds numbers (for further discussion see Sect. 11.3.3).

The total moment due to the normal stress can be similarly expressed, of which the details is omitted here. We just observe that since the $i$-component of $\boldsymbol{M}_{\Pi}$ is

$$M_{\Pi i}=\int_{\partial B}\boldsymbol{e}_i\cdot(\boldsymbol{x}\times\boldsymbol{n})\Pi\,\mathrm{d}S,$$

one simply needs to replace the harmonic function $\widehat{\phi}_i$ by a potential $\widehat{\chi}_i$ that would be induced in an inviscid fluid by rotation of $\partial B$ at unit angular velocity about an axis through the origin in the $i$-direction. Namely, $\widehat{\chi}_i$ satisfies the boundary condition (Quartapelle and Napolitano 1983)

$$\boldsymbol{n}\cdot\nabla\widehat{\chi}_i=(\boldsymbol{x}\times\boldsymbol{n})\cdot\boldsymbol{e}_i=\boldsymbol{n}\cdot(\boldsymbol{e}_i\times\boldsymbol{x})\quad\text{at}\quad\partial B. \quad (11.18)$$

Note that for rotating and/or deforming body $\boldsymbol{M}$ contains an extra term $\boldsymbol{M}_{\mathrm{s}}$ due to the surface-deformation stress.

Alternative to the choice $\psi_i=\widehat{\phi}_i$, it is natural to consider taking $\psi_i$ in (11.14) as the acyclic potential for the idealized irrotational flow over a body with unit velocity $\boldsymbol{e}_i=\nabla x_i$ at infinity, viewed in a frame of reference fixed to the center of $B$ which has no angular momentum. The body surface $\partial B$ may have arbitrary velocity $\boldsymbol{b}(\boldsymbol{x},t)$. Denote the harmonic basis vectors so constructed by $X_i$ (not the Lagrangian coordinates in early chapters), then instead of (2.185) we now have

$$\boldsymbol{n}\cdot\nabla X_i=0\quad\text{at}\quad\partial B, \quad (11.19a)$$

$$\boldsymbol{n}\cdot\nabla X_i=n_i\quad\text{at infinity}. \quad (11.19b)$$

Evidently $X_i$ and $\widehat{\phi}_i$ are related by

$$X_i=x_i-\widehat{\phi}_i. \quad (11.20)$$

This set of basis vectors has been used by Howe (1989, 1991, 1995), who developed a projection theory for the *total force* $\boldsymbol{F}$ exerted to rigid body by incompressible flow with uniform density.

Set $\psi_i = X_i$, the incompressible version of (11.14) reads

$$\rho \int_{V_\mathrm{f}} \frac{\partial \boldsymbol{u}}{\partial t} \cdot \nabla X_i \,\mathrm{d}V + \int_\Sigma p n_i \,\mathrm{d}S = -\rho \int_{V_\mathrm{f}} \boldsymbol{l} \cdot \nabla X_i \,\mathrm{d}V + \int_{\partial B} \boldsymbol{\tau} \cdot \nabla X_i \,\mathrm{d}S. \quad (11.21)$$

While (11.16) directly follows from the integral of normal stress over the body surface, we now use (11.1c) instead, assuming that $\Sigma$ is large enough to enclose all vorticity with negligible $|\boldsymbol{u}|^2$:

$$F_i = -\rho \frac{\mathrm{d}}{\mathrm{d}t} \int_{V_\mathrm{f}} u_i \,\mathrm{d}V - \int_\Sigma p n_i \,\mathrm{d}S. \quad (11.22)$$

A combination of (11.21) and (11.22) eliminates the pressure integral and introduces $F_i$. To simplify the result, we transform the unsteady term in (11.21). After dropping all surface integrals over $\Sigma$, we find

$$\int_{V_\mathrm{f}} X_{i,j} u_{j,t} \,\mathrm{d}V = \frac{\mathrm{d}}{\mathrm{d}t} \int_{V_\mathrm{f}} u_i \,\mathrm{d}V - \frac{\mathrm{d}}{\mathrm{d}t} \int_{\partial B} \widehat{\phi}_i u_n \,\mathrm{d}S - \int_{\partial B} u_n \frac{\mathrm{D}X_i}{\mathrm{D}t} \mathrm{d}S,$$

where $\widehat{\phi}_i$ is the potential used before. Thus, we arrive at a general force formula found by Howe (1995):

$$F_i = -\rho \frac{\mathrm{d}}{\mathrm{d}t} \int_{\partial B} \widehat{\phi}_i u_n \,\mathrm{d}S - \rho \int_{\partial B} \frac{\mathrm{D}X_i}{\mathrm{D}t} u_n \,\mathrm{d}S + \rho \int_{V_\mathrm{f}} \boldsymbol{l} \cdot \nabla X_i \,\mathrm{d}V - \int_{\partial B} \boldsymbol{\tau} \cdot \nabla X_i \,\mathrm{d}S. \quad (11.23)$$

In particular, for a rigid body moving with uniform velocity $\boldsymbol{b} = \boldsymbol{U}(t)$ the second integral in (11.23) vanishes; thus we obtain a decomposition very similar to (11.17) but now for the entire total force:

$$F_i = -M_{ij} \dot{U}_j + \rho \int_{V_\mathrm{f}} (\boldsymbol{\omega} \times \boldsymbol{v}) \cdot \nabla X_i \,\mathrm{d}V - \int_{\partial B} (\mu \boldsymbol{\omega} \times \boldsymbol{n}) \cdot \nabla X_i \,\mathrm{d}S. \quad (11.24)$$

Subtracting (11.17) from (11.24) should give the force due to skin friction, i.e., the integral of $\boldsymbol{\tau}$ over $\partial B$. This can indeed be verified.

For the total moment, similar to (11.18) but corresponding to $X_i$, the basis vectors for projection is taken as (Howe 1995)

$$\nabla Y_i \equiv \boldsymbol{e}_i \times \boldsymbol{x} - \nabla \widehat{\chi}_i. \quad (11.25)$$

Howe (1995) has applied (11.23) to re-derive several classic results at high and low Reynolds numbers. These include airfoil lift, induced drag, rolling and yawing moment (within the lifting-line theory), drag due to Kármán vortex street and on small sphere and bubble.

### 11.2.2 Diagnosis of Pressure Force Constituents

Owing to the fast decay of $\nabla \widehat{\phi}_i$, the projection theory for externally unbounded flow can be used to practically diagnose flow data obtained in a

*finite but sufficiently large* domain. In addition to the replacement of pressure force by local dynamic processes, this is another advantage of the projection theory. Equation (11.16) has been applied by Chang et al. (1998) to analyze the numerical results of several typical separated flows in transonic–supersonic regime. In the frame fixed to the body moving with $\boldsymbol{U} = -U\boldsymbol{e}_x$, they found that the dominant source elements of $\boldsymbol{F}_{\Pi}$ are

$$R(\boldsymbol{x}) = -\frac{1}{2}q^2\nabla\rho\cdot\nabla\phi, \tag{11.26a}$$

$$V(\boldsymbol{x}) = \rho(\boldsymbol{\omega}\times\boldsymbol{u})\cdot\nabla\phi \tag{11.26b}$$

with $\phi = U_i\widehat{\phi}_i$, which contribute to 95% or more of the total drag and lift. The positive or negative contributions to the lift and drag of major flow structures (shear layers, vortices, and shock waves) via $V(\boldsymbol{x})$ and $R(\boldsymbol{x})$ can be clearly identified. We cite two examples here. The first is a steady supersonic turbulent flow over a sphere, computed by Reynolds-average Navier–Stokes equations. The key structures are shown in Fig. 11.4.

It was found that the computational domain needs a radius of 17–22 diameters of the sphere to make the contribution to $\boldsymbol{F}_{\Pi}$ of the flow outside the domain negligible. Denote the drag coefficients due to $R(\boldsymbol{x})$ and $V(\boldsymbol{x})$ by $C_{\mathrm{DR}}$ and $C_{\mathrm{DV}}$, respectively. Their variation as free-stream Mach number $M_\infty$ is shown in Fig. 11.5. As $M_\infty$ increases, $R(\boldsymbol{x})$ due to density gradient

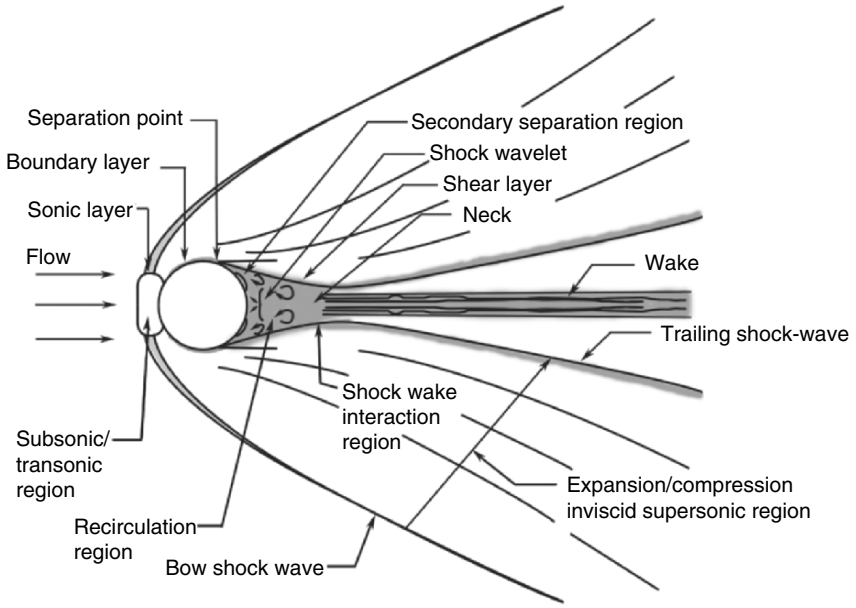


**Fig. 11.4.** Typical flow pattern of a supersonic flow around a sphere. Reproduced from Chang and Lei (1996a)

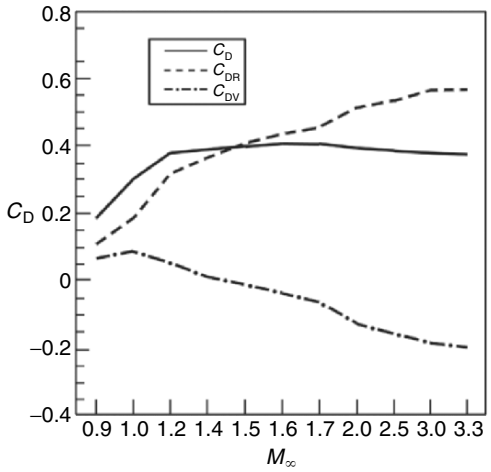


**Fig. 11.5.** Variation of $C_{\mathrm{D}}$, $C_{\mathrm{DR}}$ and $C_{\mathrm{DV}}$ with $M_\infty$ for supersonic flow over a sphere. Based on Chang and Lei (1996a)

is progressively important relative to $V(\boldsymbol{x})$ due to vorticity. It is well known that the drag reaches a maximum at a transonic Mach number; remarkably, Fig. 11.5 provides an interpretation of this phenomenon: the decrease of $C_{\mathrm{D}}$ as $M_\infty$ further increases is due to the fact that the contribution of the Lamb vector to the axial force changes from a drag to a thrust.

The second numerical example is steady flow over a slender delta wing with sweeping angle of 70° and an elliptic cross-section of the axis ratio 14:1. $M_\infty$ varies from 0.6 to 1.8, and the angle of attack $\alpha$ varies from 5° to 19°. The flow relative to the leading edge is still subsonic so in a transonic range vortices may still be the major source of lift and drag, see the sketch of Fig. 7.6. Figure 11.6 shows the situation by plotting the variation of $C_{\mathrm{LV}}$ and $C_{\mathrm{LR}}$ as $\alpha$ at two values of $M_\infty$. Also shown in the figure is the separate contribution to $C_{\mathrm{LV}}$ of the vorticity on windside ($C_{\mathrm{LV}(w)}$) and leeside ($C_{\mathrm{LV}(l)}$) of the wing surface, indicating that $V(\boldsymbol{x})$ on windside always contributes a negative vortical lift, which at a special Mach number $M_\infty = 1.2$ just cancels the positive contribution of $V(\boldsymbol{x})$ at wing side and leads to $C_{\mathrm{LV}} \simeq 0$. This behavior involves the relative orientation of $\boldsymbol{u}$, $\boldsymbol{\omega}$, and $\nabla\phi$ in different regions of the flow (for detailed analysis see Chang and Lei (1996b)).

## 11.3 Vorticity Moments and Classic Aerodynamics

The vorticity moment theory is the first version of the derivative-moment type of theories in aerodynamics, applied to a moving body $B$ in an incompressible fluid with uniform density. Assuming the external boundary $\Sigma$ retreats to

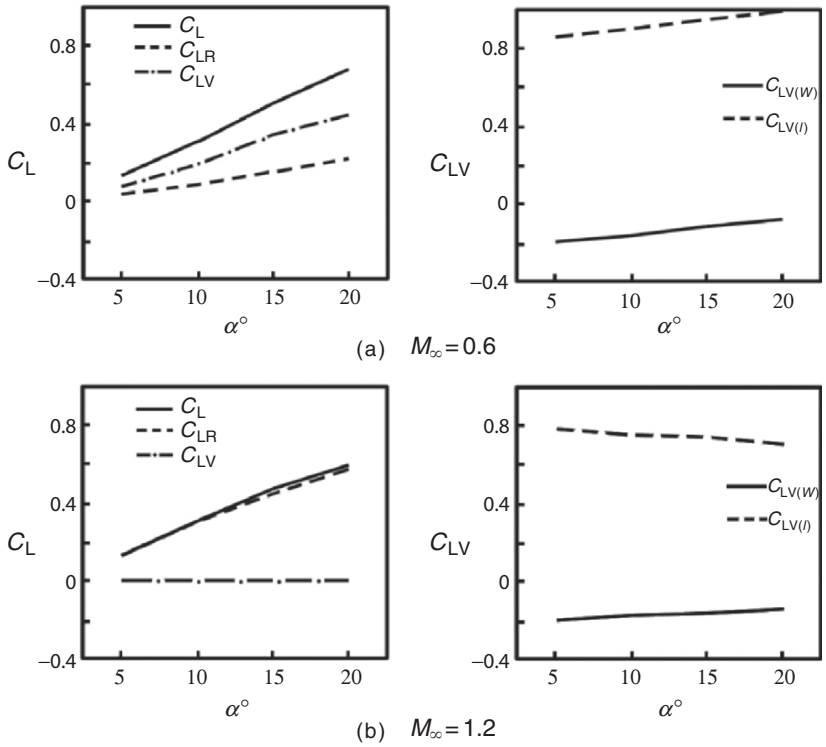


**Fig. 11.6.** Variation of $C_{\mathrm{L}}$, $C_{\mathrm{LV}}$, $C_{\mathrm{LR}}$, and $C_{\mathrm{LV}(w)}$ and $C_{\mathrm{LV}(l)}$ as $\alpha$ for transonic flow over a slender delta wing. (**a**) $M_\infty = 0.6$. (**b**) $M_\infty = 1.2$. Based on Figs. 8 and 11 of Chang and Lei (1996b)

infinity where the fluid is at rest, the theory casts $\boldsymbol{F}$ and $\boldsymbol{M}$ to the rate of change of the vortical impulse $\boldsymbol{I}$ and angular impulse $\boldsymbol{L}$ defined by (3.78) and (3.79), respectively. Thus, it represents a *global view*. Since $V_{\mathrm{f}}$ must include the starting vortex system (cf. Fig. 3.5c) and as the body keeps moving the wake region must grow, the flow in $V_{\mathrm{f}}$ is *inherently unsteady*. In this section we derive the theory, discuss its physical implication and exemplify its application, and then show how it reduces to the classic "inviscid" aerodynamics theory. Useful identities for derivative-moment transformation are listed in Sect. A.2.2.

### 11.3.1 General Formulation

For generality and better understanding, we first examine the force and moment under a weaker assumption than that stated above: The flow is irrotational at and near its external boundary $\Sigma$, so that $\boldsymbol{\omega}$, $\nabla \times \boldsymbol{\omega}$, and $\boldsymbol{l} = \boldsymbol{\omega} \times \boldsymbol{u}$ vanish on $\Sigma$. We then start from the standard force formula (11.1b), where the acceleration integral can be expressed by identity (3.117a) or (3.117b),

each representing a derivative-moment transformation. From both we have obtained the rate of change of the vortical impulse for any material volume $\mathcal{V}$ as given by (3.118). Now, set $\mathcal{D} = V_\mathrm{f}$ with $\partial V_\mathrm{f} = \partial B + \Sigma$ in (3.117b) and substitute the result into (11.1b). Since under the assumed condition on $\Sigma$ there is $\rho \boldsymbol{a} = -\nabla p$ there, by the derivative-moment transformation identity (A.25) the pressure term in (11.1b) is exactly canceled. Hence, it follows that

$$\boldsymbol{F} = -\frac{\rho}{k}\int_{V_\mathrm{f}} \boldsymbol{x} \times \boldsymbol{\omega}_{,t}\,\mathrm{d}V - \int_{V_\mathrm{f}} \boldsymbol{l}\,\mathrm{d}V + \frac{\rho}{k}\int_{\partial B} \boldsymbol{x} \times [\boldsymbol{n} \times (\boldsymbol{a}_B - \boldsymbol{l})]\,\mathrm{d}S, \quad (11.27)$$

where and below $k = n - 1$ and $n = 2, 3$ is the spatial dimensionality, $\boldsymbol{a}_B = \mathrm{D}\boldsymbol{b}/\mathrm{D}t$ is the acceleration of the body surface due to adherence, and

$$\boldsymbol{n} \times \boldsymbol{l} = \boldsymbol{\omega} u_n - \boldsymbol{u}\omega_n. \quad (11.28)$$

Thus, by the Reynolds transport theorem (2.35b), we obtain

$$\boldsymbol{F} = -\rho\frac{\mathrm{d}\boldsymbol{I}_f}{\mathrm{d}t} - \rho\int_{V_\mathrm{f}} \boldsymbol{l}\,\mathrm{d}V + \frac{\rho}{k}\int_{\partial B} \boldsymbol{x} \times (\boldsymbol{a}_B + \boldsymbol{b}\omega_n)\,\mathrm{d}S, \quad (11.29)$$

where $\boldsymbol{I}_\mathrm{f}$ is for volume $V_\mathrm{f}$. On the other hand, set $\mathcal{D} = B$ in (3.117b) and notice that the outward unit normal of $\partial B$ is $-\boldsymbol{n}$ (Fig. 11.1), since $B$ is a material body, by (2.35b) we have

$$\frac{\mathrm{d}}{\mathrm{d}t}\int_B \boldsymbol{b}\,\mathrm{d}V = \frac{\mathrm{d}\boldsymbol{I}_B}{\mathrm{d}t} + \frac{1}{k}\int_{\partial\mathcal{B}} \boldsymbol{x} \times (\boldsymbol{n} \times \boldsymbol{a}_B + \boldsymbol{b}\omega_n)\,\mathrm{d}S.$$

Comparing this with (11.29) yields

$$\boldsymbol{F} = -\rho\frac{\mathrm{d}\boldsymbol{I}_V}{\mathrm{d}t} - \rho\int_V \boldsymbol{l}\,\mathrm{d}V + \rho\frac{\mathrm{d}}{\mathrm{d}t}\int_B \boldsymbol{b}\,\mathrm{d}V, \quad (11.30)$$

where $V = V_\mathrm{f} + B$ has only an external boundary $\Sigma$. This "nonstandard" formula tells that if $\Sigma$ does not cut through any rotational-flow region then the total force has three sources: the rate of change of the impulse of domain $V_\mathrm{f} + B$, the *vortex force* given by the Lamb-vector integral (which has long been known; e.g., Saffman (1992)), and the inertial force of the virtual fluid displaced by the body.

We now shift $\Sigma$ to infinity so that $V = V_\infty$. In this case the vortex force vanishes due to the kinematic result (3.72).[6] Hence, (11.30) reduces to

$$\boldsymbol{F} = -\rho\frac{\mathrm{d}\boldsymbol{I}_\infty}{\mathrm{d}t} + \rho\frac{\mathrm{d}}{\mathrm{d}t}\int_B \boldsymbol{b}\,\mathrm{d}V. \quad (11.31)$$

[6] Recall that in deriving (3.72) and (3.73) use has been made of the asymptotic far-field behavior of the irrotational velocity.

A similar approach to the moment based on (11.2b), using derivative-moment transformation identities (A.24a) and (A.28a) as well as (3.73), yields

$$\boldsymbol{M} = -\rho \frac{\mathrm{d}\boldsymbol{L}_\infty}{\mathrm{d}t} + \rho \frac{\mathrm{d}}{\mathrm{d}t} \int_B \boldsymbol{x} \times \boldsymbol{b} \, \mathrm{d}V. \tag{11.32}$$

When $B$ is a flexible body, its interior velocity distribution may not be easily known. In that case, it is convenient to replace the body-volume integrals in (11.31) and (11.32) by the rate of change of identities (3.80) and (3.81a) applied to $B$. This yields

$$\boldsymbol{F} = -\rho \frac{\mathrm{d}\boldsymbol{I}_\mathrm{f}}{\mathrm{d}t} + \frac{\rho}{k} \frac{\mathrm{d}}{\mathrm{d}t} \int_{\partial B} \boldsymbol{x} \times (\boldsymbol{n} \times \boldsymbol{b}) \, \mathrm{d}S, \tag{11.33}$$

$$\boldsymbol{M} = \frac{\rho}{2} \frac{\mathrm{d}\boldsymbol{L}_\mathrm{f}}{\mathrm{d}t} - \frac{\rho}{2} \frac{\mathrm{d}}{\mathrm{d}t} \int_{\partial B} x^2 \boldsymbol{n} \times \boldsymbol{b} \, \mathrm{d}S, \tag{11.34}$$

where only the body-surface velocity needs to be known.

Equations (11.31–11.34) are the basic formulas of the vorticity-moment theory (Wu 1981, 2005). Recall that at the end of Sect. 3.5.2 we have shown that $\boldsymbol{I}_\infty$ and $\boldsymbol{L}_\infty$ of an unbounded fluid at rest at infinity is time invariant, even if the flow is not circulation-preserving. This invariance, however, was obtained under an implicit assumption that no vorticity-creation mechanism exists in $V_\infty$. Saffman (1992) has shown that a distributed nonconservative body force in $V_\infty$ will make $\boldsymbol{I}_\infty$ and $\boldsymbol{L}_\infty$ no longer time-invariant. Now, $V_\mathrm{f}$ is bounded internally by the solid body $B$, of which the motion and deformation is the only source of the vorticity in $V_\infty$; in this sense it has the same effect as a nonconservative body force. Then the variation of $\boldsymbol{I}_\infty$ and $\boldsymbol{L}_\infty$ caused by the body motion just implies a force and moment to $B$ as reaction. A clearer picture of this reaction to vorticity creation at body surface will be discussed in Sect. 11.4.

An interesting property of the vorticity moment theory is the *linear dependence* of $\boldsymbol{F}$ and $\boldsymbol{M}$ on $\boldsymbol{\omega}$ due to the disappearance of vortex force and moment. Hence, they can be equally applied to the total force and moment acting to a set of multiple moving bodies (Wu 1981), but not that on an individual body of the set. This property makes the theory very similar to the corresponding theory for potential flow, see (2.183) and (2.184), which by nature is always linear. The analogy between (11.31) and (2.183), and likewise for the moment, becomes perfect if $\boldsymbol{b}$ is constant so that in the former the integrals over $B$ are absent.

Except the unique property of linear dependence on vorticity, the vorticity moment theory exhibits some features common to all derivative-moment based theories. Firstly, owing to the integration by parts in derivative-moment transformation, the new integrands (in the present theory, the first and second moments of $\boldsymbol{\omega}$) do not represent the local density of momentum and angular

momentum. Rather, they are *net contributors* to $\boldsymbol{F}$ and $\boldsymbol{M}$. The entire potential flow, which occupies a much larger region in the space, is filtered out by the transformation and no longer needs to be one's concern (its effect on the vorticity advection, of course, is included implicitly).

Secondly, the new integrands have significant peak values only in considerably smaller local regions due to the exponential decay of vorticity at far field. This is a remarkable focusing, a property also shared by the projection theory.

Thirdly, since the derivative-moment transformation makes the new local integrands $\boldsymbol{x}$-dependent, if the same amount of vorticity, say, locates at larger $|\boldsymbol{x}|$, then its effect is amplified, and vice versa. This *amplification effect* by $\boldsymbol{x}$ further picks up fewer vortical structures that are crucial to $\boldsymbol{F}$ and $\boldsymbol{M}$.[7]

### 11.3.2 Force, Moment, and Vortex Loop Evolution

The core physics of vorticity moment theory and its special forms have been known to many researchers for long time (cf. Lighthill 1986a,b). Because under the assumed condition the total vorticity (total circulation if $n = 2$) is zero, the vorticity tubes created by the body motion and deformation must form closed loops (vortex couples for $n = 2$). Thus, if the circulation $\Gamma$ and motion of a vortex loop or couple are known, then so is their contribution to the force and moment. The problem is particularly simple in the Euler limit with $\mathrm{d}\Gamma/\mathrm{d}t = 0$.

von Kármán and Burgers (1935) have essentially used (11.31) to give a simple derivation of the Kutta–Joukwski formula (11.6). Consider the two-dimensional vortex couple introduced in Sect. 3.4.1, see (3.87) and Fig. 3.12. Let $\Gamma < 0$ be the circulation of the *bound vortex* of the airfoil in an oncoming flow $\boldsymbol{U} = U\boldsymbol{e}_x$, and assume the near-field flow is steady. As shown in Sect. 4.4.2, in this case no vortex wake sheds off. Thus, $-\Gamma > 0$ must be the circulation of the starting vortex alone, which retreats with speed $U$. The separation $r$ of the vortex couple then increases with the rate $\mathrm{d}r/\mathrm{d}t = U$, and hence (11.6) follows at once.

In three dimensions, as shown by (3.88), (3.89), and Fig. 3.13, the impulse and angular impulse caused by a thin vortex loop $C$ of circulation $\Gamma$ are precisely the vectorial area spanned by the loop and the moment of vectorial

[7] The origin of the position vector (which has been set zero here and below) can be arbitrarily chosen (a general proof is given in Sect. A.2.3). Hence whether a local vortical structure has favorable contribution to total force also depends on the subjective choice of the origin. But one can always make a convenient choice such that the flow diagnosis is most intuitive. See the footnote following (11.54a,b) below.

surface element, respectively. Hence a single evolving vortex loop will contribute a force and moment

$$\boldsymbol{F} = -\rho\Gamma\frac{\mathrm{d}}{\mathrm{d}t}\int_S \mathrm{d}\boldsymbol{S}, \tag{11.35}$$

$$\boldsymbol{M} = -\frac{2}{3}\rho\Gamma\frac{\mathrm{d}}{\mathrm{d}t}\int_S \boldsymbol{x}\times\mathrm{d}\boldsymbol{S}. \tag{11.36}$$

For a flow over a three-dimensional wing of span $b$ with constant velocity $\boldsymbol{U} = U\boldsymbol{e}_x$, a remote observer will see such a single vortex loop sketched in Fig. 3.5c. Then the rate of change of $\boldsymbol{S}$ equals $-bU\boldsymbol{e}_z$, solely due to the continuous generation of the vorticity from the body surface. Therefore, (11.35) gives

$$\boldsymbol{F} \simeq \rho\boldsymbol{U}\times\boldsymbol{\Gamma}b, \tag{11.37}$$

which is asymptotically accurate for a rectangular wing with constant chord $c$ and $b\to\infty$; each wing section of unit thickness will then have a lift given by (11.6).

Better than (11.37), we may replace the single pair of vorticity tubes with distance $b$ by distributed $\omega_x(y,z)$ in the wake vortices, which correspond to a bundle of vortex loops. This leads to

$$L \simeq \rho U\int_W y\omega_x\,\mathrm{d}S, \tag{11.38}$$

where $W$ is a $(y,z)$-plane cutting through the wake (cf. Fig. 11.20). Then, if $\omega_x$ is confined in a thin flat vortex sheet with strength $\gamma(y)$ as in the lifting-line theory (Fig. 11.3), by a one-dimensional derivative-moment transformation and (11.9) there is

$$y\gamma = \Gamma - \frac{\mathrm{d}(y\Gamma)}{\mathrm{d}y}.$$

Substituting this into (11.38) and noticing $\Gamma = 0$ at $y = \pm s$, we recover (11.7a) at once.

The multiple vortex-loop argument has been used by Wu et al. (2002) in analyzing various constituents of the force and moment on a helicopter rotor. An interesting application of (11.31) is given by Sun and Wu (2004) in a simulation of insect flight. Insects may fly at a Reynolds number as small as of 100, for which the lift predicted by classic steady wing theory is far lower than needed for supporting the insect weight. The crucial role of unsteady motion of lifting vortices was experimentally discovered only recently (e.g., Ellington et al. 1996). To further understand the physics, Sun and Wu conducted a Navier–Stokes computation of a thin wing which rotates azimuthally by 160° at constant angular velocity and angle of attack after an initial start, see Fig. 11.7. Numerical tests have confirmed that to a great extent this model can well mimic a down- or upstroke of the flapping motion of insect wings, yielding lift $L$ and drag $D$ in good agreement with experimental results.

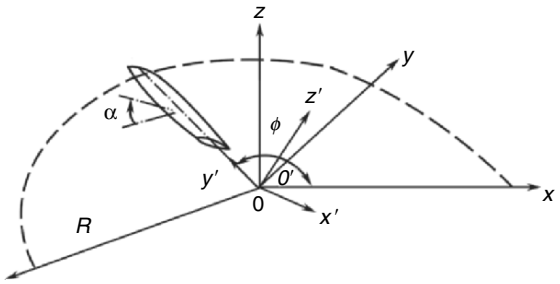


**Fig. 11.7.** Rotating wing; fixed $(x, y, z)$ frame and rotating $(x', y', z')$ frame. From Sun and Wu (2004)

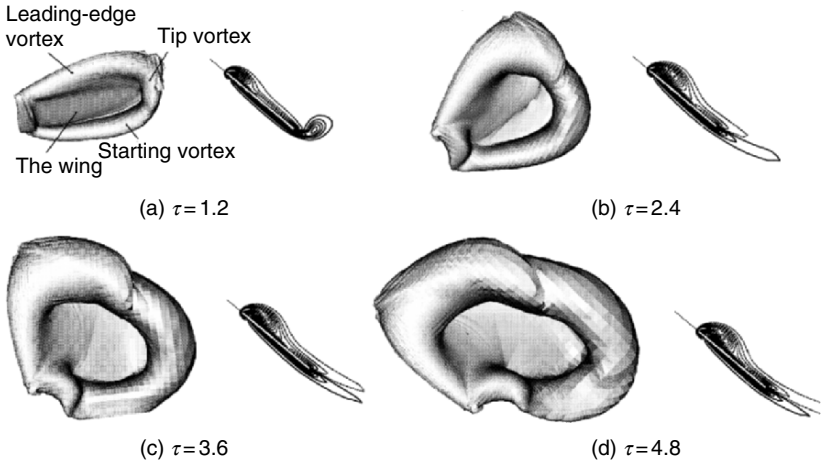


**Fig. 11.8.** Time evolution of isovorticity surface (*left*) around the wing and contours of $\omega_{y'}$ at wing section $0.6R$. From Sun and Wu (2004)

Sun and Wu (2004) found that $L$ and $D$ computed from (11.31) is in excellent agreement with that obtained by (11.1a). Figure 11.8 shows the isovorticity surface and the contours of $\omega_{y'}$ at wing section $0.6R$ ($R$ is the semi wingspan) and different dimensionless time $\tau$. A strong separated vortex *remains attached* to the leading edge in the whole period of a single stroke, which connects to a wingtip vortex, a wing root vortex, and a starting vortex to form a closed loop. As the wing rotates, the vector surface area spanned by the loop increases almost linearly and the loop is roughly on an inclined plane. Therefore, almost constant $L$ and $D$ are produced after start. The authors further found that the key mechanism for the leading-edge vortex to remain attached is a spanwise pressure gradient (at $Re = 800$ and 3,200), and its joint effect with centrifugal force (at $Re = 200$). Similar

to the leading-edge vortices on slender wing (Chap. 7), now these spanwise forces advect the vorticity in leading-edge vortex to the wingtip to avoid oversaturation and shedding.

### 11.3.3 Force and Moment on Unsteady Lifting Surface

Various classic external aerodynamic theories can be deduced from the vorticity moment theory in a unified manner at different approximation levels. This theoretical unification is a manifestation of the physical fact that all incompressible force and moment are from the same vortical root. We demonstrate this in the Euler limit.

The simplest situation is the force and moment due purely to body acceleration, for which (11.33) and (11.34) should reduce to (2.183) and (2.184) but with viscous interpretation. The body acceleration creates an unsteady boundary layer attached to $\partial B$ but inside $V_{\rm f}$, of which the effect is in $\boldsymbol{I}_{\rm f}$ and $\boldsymbol{L}_{\rm f}$. Namely, *an accelerating body must be dressed in an acyclic attached vortex layer*. Let $\widehat{\boldsymbol{n}} = -\boldsymbol{n}$ be the unit normal of $\partial B$ pointing into the fluid, in the Euler limit this layer becomes a vortex sheet of strength

$$\boldsymbol{\gamma}_{\rm ac} = \widehat{\boldsymbol{n}} \times [\![\boldsymbol{u}]\!] = \widehat{\boldsymbol{n}} \times (\nabla \phi_{\rm ac} - \boldsymbol{b}), \tag{11.39}$$

where suffix ac denotes acyclic and $\phi_{\rm ac}$ can be solved from (2.173) solely from the specified body-surface velocity $\boldsymbol{b}(\boldsymbol{x}, t)$. Then

$$\boldsymbol{I}_{\rm f} = \frac{1}{k} \int_{\partial B} \boldsymbol{x} \times \boldsymbol{\gamma}_{\rm ac} \, {\rm d}S = \frac{1}{k} \int_{\partial B} \boldsymbol{x} \times [\widehat{\boldsymbol{n}} \times (\nabla \phi_{\rm ac} - \boldsymbol{b})] \, {\rm d}S.$$

Here, after being substituted into (11.33), the integral of $\boldsymbol{b}$ is canceled, while like (3.84) the integral of $\phi_{\rm ac}$ is cast to

$$\frac{1}{k} \int_{\partial B} \boldsymbol{x} \times (\widehat{\boldsymbol{n}} \times \nabla \phi_{\rm ac}) \, {\rm d}S = - \int_{\partial B} \phi_{\rm ac} \widehat{\boldsymbol{n}} \, {\rm d}S = \boldsymbol{I}_{\phi}.$$

Thus, along with a similar approach to $\boldsymbol{L}_{\rm f}$, in (11.33) and (11.34) what remains is just (2.183) and (2.184):

$$\boldsymbol{F}_{\rm ac} = -\rho \frac{{\rm d}\boldsymbol{I}_{\phi}}{{\rm d}t}, \quad \boldsymbol{M}_{\rm ac} = -\rho \frac{{\rm d}\boldsymbol{L}_{\phi}}{{\rm d}t}.$$

Therefore, denote the impulse and angular impulse of $V_{\rm f}$ excluding the contribution of $\boldsymbol{\gamma}_{\rm ac}$ by $\boldsymbol{I}_{\rm f^-}$ and $\boldsymbol{L}_{\rm f^-}$, respectively, the force and moment can be simply expressed by

$$\boldsymbol{F} = -\rho \frac{\rm d}{{\rm d}t} (\boldsymbol{I}_{\rm f^-} + \boldsymbol{I}_{\phi}), \tag{11.40}$$

$$\boldsymbol{M} = -\rho \frac{\rm d}{{\rm d}t} (\boldsymbol{L}_{\rm f^-} + \boldsymbol{L}_{\phi}), \tag{11.41}$$

with the understanding that $\phi_{\rm ac}$ has influence on the vorticity advection.

We digress to note that the concept of vortex sheet can well be applied to flow at finite Reynolds numbers, as explained by Wu (2005). During a small time interval $\delta t$, the body-surface acceleration $\boldsymbol{a}_B$ causes a velocity increment $\delta \boldsymbol{b} = \boldsymbol{a}_B \delta t$, which by (11.39) yields a vortex layer of strength $\delta \boldsymbol{\gamma}_{\rm ac}$, so that the rate of change of $\boldsymbol{\gamma}_{\rm ac}$ is proportional to $\boldsymbol{a}_B$. This picture becomes exact as $\delta t \to 0$ no matter if $Re \to \infty$. Wu (2005) has demonstrated that, by substituting this $\delta \boldsymbol{\gamma}_{\rm ac}$ into (11.33), one obtains exactly the same $\boldsymbol{F}_{\rm ac}$ as calculated by the virtual mass approach based on inviscid potential-flow theory (Sect. 2.4.4).

Having clarifying the role of body-surface acceleration, we now focus on the rest part of force and moment caused by attached vortex sheet with nonzero circulation and free vortex sheet in the wake, denoted by suffix $\gamma$. We consider a thing wing represented by a bound vortex sheet or *lifting surface* as in Sect. 4.4.1. The interest in unsteady *flexible lifting surface theory* has recently revived due to the need for a theoretical basis of studying thin fish swimming and animal flight (Wu 2002).

In the Euler limit, the expressions of $\boldsymbol{I}$ and $\boldsymbol{L}$ and their rates of change have been given by (4.136–4.139), with vanishing Lamb-vector integrals. From these and (4.133) that tells how an unsteady bound vortex sheet induces a pressure jump $[\![p_\gamma]\!]$:

$$-[\![p_\gamma]\!]\boldsymbol{n} = \rho \boldsymbol{n} \frac{{\rm D}\Gamma}{{\rm D}t} = \rho \left( \bar{\boldsymbol{u}}_\pi \times \boldsymbol{\gamma}_{\rm b} + \frac{\partial \Gamma}{\partial t} \boldsymbol{n} \right),$$

we obtain the force and moment on a rigid or flexible lifting surface:

$$\boldsymbol{F}_\gamma = -\int_{S_{\rm b}} [\![p_\gamma]\!] \boldsymbol{n} \, {\rm d}S = \rho \int_{S_{\rm b}} \frac{{\rm D}\Gamma}{{\rm D}t} \boldsymbol{n} \, {\rm d}S \tag{11.42a}$$

$$= \rho \int_{S_{\rm b}} \bar{\boldsymbol{u}}_\pi \times \boldsymbol{\gamma}_{\rm b} \, {\rm d}S + \rho \int_{S_{\rm w}} \frac{\partial \Gamma}{\partial t} \boldsymbol{n} \, {\rm d}S, \tag{11.42b}$$

$$\boldsymbol{M}_\gamma = -\int_{S_{\rm w}} [\![p_\gamma]\!] \boldsymbol{x} \times \boldsymbol{n} \, {\rm d}S = \rho \int_{S_{\rm b}} \frac{{\rm D}\Gamma}{{\rm D}t} \boldsymbol{x} \times \boldsymbol{n} \, {\rm d}S \tag{11.43a}$$

$$= \rho \int_{S_{\rm b}} \boldsymbol{x} \times (\bar{\boldsymbol{u}}_\pi \times \boldsymbol{\gamma}_{\rm b}) \, {\rm d}S + \rho \int_{S_{\rm b}} \frac{\partial \Gamma}{\partial t} \boldsymbol{x} \times \boldsymbol{n} \, {\rm d}S, \tag{11.43b}$$

where $S_{\rm b}$ is the area of the bound vortex sheet, i.e., the wing area. These formulas are the basis of unsteady *lifting-surface theory*, which clearly reveal the vortical root of pressure jump on a wing.

Then, in linearized approximation, the vortex sheet has known location as we saw in the lifting-line theory. This greatly simplifies the above formulas and leads one back to almost entire classic wing aerodynamics. For example, it is easily verified that, the three-dimensional steady version of (11.42) returns to (11.7), while its two-dimensional unsteady version returns to the oscillating-airfoil theory. For details of these classic theories see, e.g., Prandtl and Tietjens (1934), Glauert (1947), Bisplinghoff et al. (1955), and Ashley and Landahl (1965).

## 11.4 Boundary Vorticity-Flux Theory

Opposite to the global view implied by the vorticity moment theory, we now trace the physical root to the body surface, where the entire vorticity field is produced. Then, the derivative-moment transformation leads to the *boundary vorticity-flux theory* as an *on-wall close view*.

### 11.4.1 General Formulation

Return to the incompressible flow problem stated in Sect. 11.1.1 (See Fig. 11.1), but now start from (11.1a) and (11.2a) where $\boldsymbol{F}$ and $\boldsymbol{M}$ are expressed by the body-surface integrals of the on-wall stress $\boldsymbol{t}$ and its moment, respectively. Naturally, the desired local dynamics on $\partial B$ that has net contribution to $\boldsymbol{F}$ and $\boldsymbol{M}$ should follow from proper transformation identities for surface integrals, which are given in Sect. A.2.3. To employ these identities we have to decompose the stress $\boldsymbol{t}$ into normal and tangent components first. Because the effect of $\boldsymbol{t}_{\rm s}$ has been integrated out, it suffices to deal with the orthogonal components of the reduced stress $\widehat{\boldsymbol{t}} = -p\boldsymbol{n} + \mu\boldsymbol{\omega} \times \boldsymbol{n}$, see (2.149). Therefore, using (A.25) and (A.26) to transform (11.1a), and using (A.28a) and (A.29) to transform (11.2a), in three dimensions we immediately obtain (Wu 1987)

$$\boldsymbol{F} = -\int_{\partial B} \rho \boldsymbol{x} \times \left( \frac{1}{2}\boldsymbol{\sigma}_{\rm p} + \boldsymbol{\sigma}_{\rm vis} \right) {\rm d}S, \tag{11.44}$$

$$\boldsymbol{M} = \int_{\partial B} \rho \left[ \frac{1}{2} x^2 (\boldsymbol{\sigma}_{\rm p} + \boldsymbol{\sigma}_{\rm vis}) - \boldsymbol{x}\boldsymbol{x} \cdot \boldsymbol{\sigma}_{\rm vis} \right] {\rm d}S + \boldsymbol{M}_{{\rm s}B}, \tag{11.45}$$

where $\boldsymbol{\sigma}_{\rm p}$ and $\boldsymbol{\sigma}_{\rm vis}$ are the stress-related boundary vorticity fluxes defined in (4.24b), and $\boldsymbol{M}_{{\rm s}B}$ is given by (11.3a). These formulas are the main result of the boundary vorticity flux theory. If one wishes, $\boldsymbol{M}_{{\rm s}B}$ can be absorbed into the first term of (11.45) by using the full normal and tangent stresses on deformable surface, see (2.151). Therefore, we conclude that

*For three-dimensional viscous flow over a solid body or a body of different fluid performing arbitrary motion, a body surface element has net contribution to the total force and moment only if the stress-related boundary vorticity fluxes are nonzero on the element.*

For example, for flow over sphere of radius $R$ at $Re \ll 1$, the Stokes drag law (4.59) can be quickly inferred from (11.44) by the vorticity distribution (4.57a) alone, which has led to (4.60a).[8] Thus, (4.59) follows at once, indicating that the pressure force and skin-friction force provide 1/3 and 2/3 of the total drag, respectively. On the other hand, by (11.45), for flow over any non-rotating sphere at *arbitrary* $Re$, we simply have

$$\boldsymbol{M} = \frac{1}{2}\rho R^2 \int_{\partial B} (\boldsymbol{\sigma}_{\rm p} + \boldsymbol{\sigma}_{\rm vis})\, {\rm d}S,$$

[8] This involves only the near-wall vorticity distribution, regardless the failure of the Stokes solution at far field.

where by (4.24b) both $\boldsymbol{\sigma}_{\rm p}$ and $\boldsymbol{\sigma}_{\rm vis}$ are under the operator $\boldsymbol{n}\times\nabla$ and hence integrate to zero by the generalized Stokes theorem. Thus the sphere is moment-free as it should. But if the sphere rotates the entire vorticity field will be redistributed, and there will be a nonzero moment

$$\boldsymbol{M} = \mu R^2 \int_{\partial B} \boldsymbol{e}_R \nabla_\pi \cdot \boldsymbol{\omega}\, {\rm d}S - \frac{8\pi R^3}{3}\mu\boldsymbol{\Omega}.$$

The theory can be easily generalized in a couple of ways (Wu et al. 1988b; Wu 1995; Wu and Wu 1993, 1996). Firstly, a simple replacement of pressure $p$ by $\mathit{\Pi} = p - (\lambda + 2\mu)\vartheta$ immediately extends the theory to viscous compressible flow with constant $\mu$. Here, expressing $\boldsymbol{F}$ and $\boldsymbol{L}$ by boundary vorticity fluxes does not conflict the dominance of the compressing process in supersonic regime. Rather, due to the viscous boundary coupling via the no-slip condition (Sect. 2.4.3), a shearing process must appear adjacent to the wall as a *byproduct* of compressing process. For example, when a shock wave hits the wall, the associated strong adverse pressure gradient will enter the boundary vorticity flux through $\boldsymbol{\sigma}_{\mathit{\Pi}}$ and hence causes a strong creation of vorticity opposite to that upstream the shock, somewhat similar to case that the interactive pressure gradient of $O(Re^{1/8})$ in the boundary-layer separation zone causes a strong peak of $\boldsymbol{\sigma}_{\rm p}$ (Sect. 5.3). In other words, *as an on-wall footprint of the flow field, the boundary vorticity flux can faithfully reflect the effect of compressing process on the wall.*

Secondly, owing to the transformation identities in Sect. A.2.3, we can consider the force and moment on an *open* surface, such as a piece of aircraft wing or body, a turbo blade, or the under-water part of a ship. This extension is done by simply adding proper line-integrals, including those due to $\boldsymbol{t}_{\rm s}$ given by (2.152a,b). Thus, for incompressible flow, we may write

$$\boldsymbol{F} = \boldsymbol{F}_{\rm surf} + \boldsymbol{F}_{\rm line}, \quad \boldsymbol{M} = \boldsymbol{M}_{\rm surf} + \boldsymbol{M}_{\rm line},$$

where $\boldsymbol{F}_{\rm surf}$ and $\boldsymbol{M}_{\rm surf}$ are given by (11.44) and (11.45), respectively, while

$$\boldsymbol{F}_{\rm line} = \frac{1}{2}\oint_{\partial S} \boldsymbol{x}\times(p\,{\rm d}\boldsymbol{x} + 2\mu\boldsymbol{\omega}\times{\rm d}\boldsymbol{x}) + 2\mu\oint_{\partial S}\boldsymbol{u}\times{\rm d}\boldsymbol{x}, \tag{11.46}$$

$$\boldsymbol{M}_{\rm line} = -\frac{1}{2}\oint_{\partial S}[x^2 p\,{\rm d}\boldsymbol{x} + (x^2\mathbf{I} - 2\boldsymbol{x}\boldsymbol{x})\cdot(\mu\boldsymbol{\omega}\times{\rm d}\boldsymbol{x})] + 2\mu\oint_{\partial S}\boldsymbol{x}\times(\boldsymbol{u}\times{\rm d}\boldsymbol{x}). \tag{11.47}$$

Note that with the help of these open-surface formulas, the $(p,\boldsymbol{\omega})$-distribution in (11.44) and (11.45) only needs to be *piecewise smooth*, because the boundary line-integral of each open piece must finally be cancelled. This is useful when the body surface has sharp edges, corners, or shock waves across which the tangent gradients of $\mathit{\Pi}$ and $\boldsymbol{\omega}$ are singular.

Thirdly, when $\mu$ is variable as in flows with extremely strong heat transfer, a simple way to generalize the preceding formulas is to take $\mu\boldsymbol{\omega}$ as a whole, including redefining the boundary vorticity flux as $\boldsymbol{\sigma}^d = \boldsymbol{n} \cdot \nabla(\mu\boldsymbol{\omega})$ so it has a dynamic dimension (denoted by superscript $d$), see Wu and Wu (1993). Moreover, since now $\nabla\cdot(2\mu\mathbf{B}) \neq \mathbf{0}$ and the local effect of $\boldsymbol{t}_\mathrm{s}$ has to be included, we should use (2.151) and define

$$\boldsymbol{\sigma}^d_{\tilde{\Pi}} \equiv \boldsymbol{n} \times \nabla\tilde{\Pi}, \quad \boldsymbol{\sigma}^d_\mathrm{vis} \equiv (\boldsymbol{n} \times \nabla) \times (\mu\boldsymbol{\omega}_r). \tag{11.48}$$

Correspondingly, (11.44) and (11.45) are extended to

$$\boldsymbol{F} = -\int_{\partial B} \boldsymbol{x} \times \left(\frac{1}{2}\boldsymbol{\sigma}^d_{\tilde{\Pi}} + \boldsymbol{\sigma}^d_\mathrm{vis}\right) \mathrm{d}S, \tag{11.49}$$

$$\boldsymbol{M} = \int_{\partial B} \left[\frac{1}{2}x^2(\boldsymbol{\sigma}^d_{\tilde{\Pi}} + \boldsymbol{\sigma}^d_\mathrm{vis}) - \boldsymbol{x}\boldsymbol{x} \cdot \boldsymbol{\sigma}^d_\mathrm{vis}\right] \mathrm{d}S, \tag{11.50}$$

where density $\rho$ as well as $\boldsymbol{M}_{\mathrm{s}B}$ in (11.45) has been absorbed into $\boldsymbol{\sigma}^d$s. This generalization makes the resulting force and moment formulas have exactly the same application range as that of the Navier–Stokes equation. Note that for variable $\mu$ the Navier–Stokes equation has an extra term, see (2.160a), which adds a viscous constituent $\boldsymbol{\sigma}^d_\mu \equiv 2\boldsymbol{n} \times (\nabla\mu \cdot \mathbf{B})$ to the boundary vorticity flux studied in Sect. 4.1.3. However, $\boldsymbol{\sigma}^d_\mu$ is not stress-related and does not explicitly enter the force and moment.

Finally, two-dimensional flow on the $(x, y)$-plane needs special treatment. We illustrate this by incompressible flow over an open deformable contour $C$ with end points $a$ and $b$. The positive direction of a boundary curve is defined by the convention that as one moves along it the fluid is kept at its left-hand side. Thus, on body surface we let $s$ increase along clockwise direction such that $(\boldsymbol{n}, \boldsymbol{e}_s, \boldsymbol{e}_z)$ form a right-hand triad. Then by (A.36) and (A.37), and noticing that the two-dimensional version of (2.152a,b) is

$$\int_a^b \boldsymbol{t}_\mathrm{s}\,\mathrm{d}s = 2\mu(v\boldsymbol{e}_x - u\boldsymbol{e}_y)|_a^b, \tag{11.51a}$$

$$\int_a^b \boldsymbol{x} \times \boldsymbol{t}_\mathrm{s}\,\mathrm{d}s = 2\mu\boldsymbol{e}_z \left[(\boldsymbol{x} \cdot \boldsymbol{u})|_a^b - \int_a^b u_\mathrm{s}\,\mathrm{d}s\right], \tag{11.51b}$$

we obtain

$$F_x = \rho\int_a^b \left(-y\sigma_\mathrm{p} + \nu x\frac{\partial\omega}{\partial s}\right) \mathrm{d}s + (yp - \mu x\omega + 2\mu v)|_a^b, \tag{11.52a}$$

$$F_y = \rho\int_a^b \left(x\sigma_\mathrm{p} + \nu y\frac{\partial\omega}{\partial s}\right) \mathrm{d}s - (xp + \mu y\omega + 2\mu u)|_a^b. \tag{11.52b}$$

Moreover, for $\boldsymbol{M} = M_z \boldsymbol{e}_z$, as observed at the end of Sect. A.2.4 it is impossible to express the boundary integral of $\boldsymbol{x} \times (\mu \boldsymbol{\omega} \times \boldsymbol{n}) = \boldsymbol{e}_z \mu \omega (\boldsymbol{x} \cdot \boldsymbol{n})$ by $\partial\omega/\partial s$. Thus by (A.38) and (11.51b), the result is

$$M_z = \rho \int_a^b \left( \frac{1}{2} x^2 \sigma_\mathrm{p} + \nu \boldsymbol{x} \cdot \boldsymbol{n} \omega \right) \mathrm{d}s - 2\mu (xu + yv)|_a^b + 2\mu \int_a^b u_\mathrm{s} \, \mathrm{d}s. \quad (11.53)$$

For a closed loop the last term is $-2\mu \Gamma_\mathrm{C}$ by our sign convention.

### 11.4.2 Airfoil Flow Diagnosis

While for Stokes flow the boundary vorticity flux distributes quite evenly, at large Reynolds numbers it typically has high peaks at very localized regions of $\partial B$, see the discussion following (4.94). It is this property in the high-$Re$ regime that makes the theory a valuable tool in flow diagnosis and control. So far it has been applied to the diagnosis of aerodynamic force on several configurations at different air speed regimes (Wu et al. 1999c), including airfoils and delta wing-body combination in incompressible flow, fairing in transonic flow, and wave rider in hypersonic flow. Zhu (2000) has demonstrated that the $\sigma_\mathrm{p}$-distribution can be posed in the objective function for optimal airfoil design.

To demonstrate the basic nature of this kind of diagnosis, we now consider the total force acting to a stationary two-dimensional airfoil by steady incompressible flow. At $Re \gg 1$ the contribution of skin friction can be neglected. In the wind-axis coordinate system $(x, y)$, (11.52) yields the lift and drag formulas

$$L = \rho \int_C x \sigma_\mathrm{p} \, \mathrm{d}s, \quad D = -\rho \oint_C y \sigma_\mathrm{p} \, \mathrm{d}s. \quad (11.54\text{a,b})$$

For convenience let the origin of $(x, y)$ be at the mid-chord point of the airfoil. Then by (11.54a) a negative $\sigma$-peak implies a positive lift for $x < 0$ and negative lift for $x > 0$. If for $x < 0$ there is a positive $\sigma$-peak on the upper surface, say, it not only produces a negative lift but also tends to cause early separation since it will be stronger as $\alpha$ increases. Moreover, the vorticity created by this unfavorable $\sigma$ adds extra enstrophy to the flow field, implying larger viscous drag. Therefore, ideally one wishes the sign of $\sigma$ over the upper surface to be like that sketched in Fig. 11.9a without front positive $\sigma$-peak and rear negative $\sigma$-peak on the upper surface.[9] In the figure the sign of $\sigma$

[9] Whether a boundary vorticity flux peak is favorable depends on the choice of the origin of the coordinates. For example, shifting the origin to the trailing edge would imply that negative boundary vorticity flux peaks on upper surface are all favorable, but by (11.54a) the contribution to the lift of a rear peak is less than that of a front one. However, this does not influence the net effect on the lift and drag, and setting the origin at the mid-chord is most convenient.

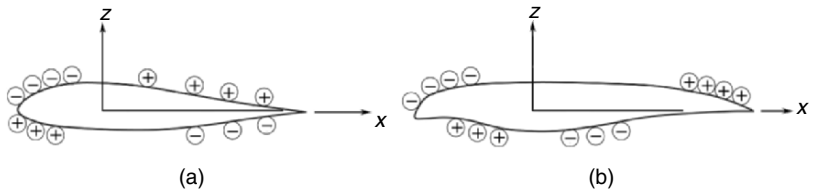


**Fig. 11.9.** Idealized boundary vorticity flux distribution over airfoil. (**a**) The boundary vorticity flux is completely favorable on upper surface. (**b**) An even more favorable boundary vorticity flux distribution

over the lower surface is qualitatively estimated by pressure gradient and the constraint

$$\oint_C \sigma_{\mathrm{p}}\,\mathrm{d}s = -\oint_C \frac{\partial p}{\partial s}\,\mathrm{d}s = 0. \tag{11.55}$$

Given the favorable sign distribution of $\sigma_{\mathrm{p}}$, however, (11.54a) indicates that there is still a room to further enhance $L$ by shifting the location of $\sigma$-peaks. On the upper surface, the front negative $\sigma$-peak and rear positive $\sigma$-peak will produce more lift if their $|x|$ is larger, while on the lower surface these peaks will produce less negative $L$ if their $|x|$ is smaller. This simple intuitive observation suggests a modification of the airfoil shape of Fig. 11.9a to that of Fig. 11.9b, which is precisely of the kind of *supercritical airfoils* originally designed for alleviating transonic wave drag. The present argument indicates that a supercritical airfoil must also have better aerodynamic performance at low Mach numbers.

Quantitatively, consider the relation between $\sigma$ and the airfoil geometry. For steady and attached airfoil flow at large $Re$, this relation can be obtained analytically in the Euler-limit by the potential-flow theory. Let $C$ be any streamline in the potential-flow region, of which the arc element $\mathrm{d}s$ has inclination angle $\chi$ with respect to the $x$-axis, see Fig. 11.10. Thus, in terms of complex variables $z = x + \mathrm{i}y$ and $w = \phi + \mathrm{i}\psi$ as used in deriving (11.10), we have

$$\begin{gathered} \mathrm{d}x = \cos\chi\,\mathrm{d}s,\ \mathrm{d}y = \sin\chi\,\mathrm{d}s,\ \ \mathrm{d}z = \mathrm{d}s\,\mathrm{e}^{\mathrm{i}\chi}, \\ u = q\cos\chi, \quad v = q\sin\chi, \quad \frac{\mathrm{d}w}{\mathrm{d}z} = q\,\mathrm{e}^{-\mathrm{i}\chi}. \end{gathered} \tag{11.56}$$

And, the tangent component of the Euler equation $C$ reads

$$a_{\mathrm{s}} = \frac{1}{2}\frac{\partial q^2}{\partial s} = -\frac{\partial p}{\partial s} \quad \text{on} \quad C. \tag{11.57}$$

Now, denote

$$\rho(z) = \log q - \mathrm{i}\chi = \log\left(\frac{\mathrm{d}w}{\mathrm{d}z}\right)$$

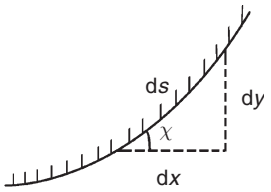


**Fig. 11.10.** Geometric relation of a contour $C$

such that

$$\frac{\mathrm{d}\rho}{\mathrm{d}z} = \frac{\mathrm{d}z}{\mathrm{d}w}\frac{\mathrm{d}^2 w}{\mathrm{d}z^2} = \frac{1}{2q^2}\frac{\mathrm{d}q^2}{\mathrm{d}z} - \mathrm{i}\frac{\mathrm{d}\chi}{\mathrm{d}z}.$$

Then by using $\mathrm{d}z = \mathrm{d}s\,\mathrm{e}^{i\chi}$ and (11.57) we find $\mathrm{e}^{i\chi}\mathrm{d}\rho/dz = q^{-2}\sigma_\mathrm{p} - \mathrm{i}\kappa$, where $\kappa \equiv \mathrm{d}\chi/\mathrm{d}s$ is the curvature of $C$. But by (11.56) $\mathrm{e}^{i\chi} = q\,\mathrm{d}z/\mathrm{d}w$, so

$$\frac{a_\mathrm{s}}{q^3} - \frac{\mathrm{i}\kappa}{q} = \left(\frac{\mathrm{d}z}{\mathrm{d}w}\right)^2 \frac{\mathrm{d}^2 w}{\mathrm{d}z^2} \quad \text{on} \quad C.$$

Therefore, $a_\mathrm{s}/q^3$ and $-\kappa/q$ are the real and imaginary parts of an analytical function (which is known once so is $\mathrm{d}w/\mathrm{d}z$).

Finally, let the streamline $C$ be the airfoil contour *underneath* the attached vortex sheet where the no-slip condition still works and $a_\mathrm{s}$ drops to zero. But the viscosity comes into play, producing a boundary vorticity flux $\sigma$ to replace $a_\mathrm{s}$ to balance the pressure gradient. Namely, we have

$$\frac{\sigma_\mathrm{p}}{q^3} - \frac{\mathrm{i}\kappa}{q} = \left(\frac{\mathrm{d}z}{\mathrm{d}w}\right)^2 \frac{\mathrm{d}^2 w}{\mathrm{d}z^2} \quad \text{on airfoil,} \tag{11.58}$$

indicating that if $q \sim 1$ then $\sigma_\mathrm{p}$, or pressure gradient, is directly linked to the local airfoil curvature.[10] But strictly the $\sigma_\mathrm{p}$–$\kappa$ relation is nonlinear and of global nature.

Equation (11.58) can be used to calculate $\sigma_\mathrm{p}$ over a realistic airfoil as long as the flow is attached. Figure 11.11a shows the $\sigma$-distribution computed thereby for a helicopter rotor airfoil VR-12 at $\alpha = 6°$, compared with the Navier–Stokes computation at $Re = 10^6$ using an one-equation turbulence model (Zhu 2000). The difference is very small except at the trailing edge, where the "inviscid" $\sigma$ approaches $\pm\infty$. But it can be shown that this singularity is symmetric and precisely canceled in (11.54).

The VR-12 airfoil has higher maximum lift before stall and larger stall angle of attack than a traditional airfoil, say NACA-0012. By (11.54a), the

[10] This result can be compared with that in the linearized supersonic aerodynamic theory, where the pressure is simply proportional to the local wall slope, as exemplified by (5.56c′).

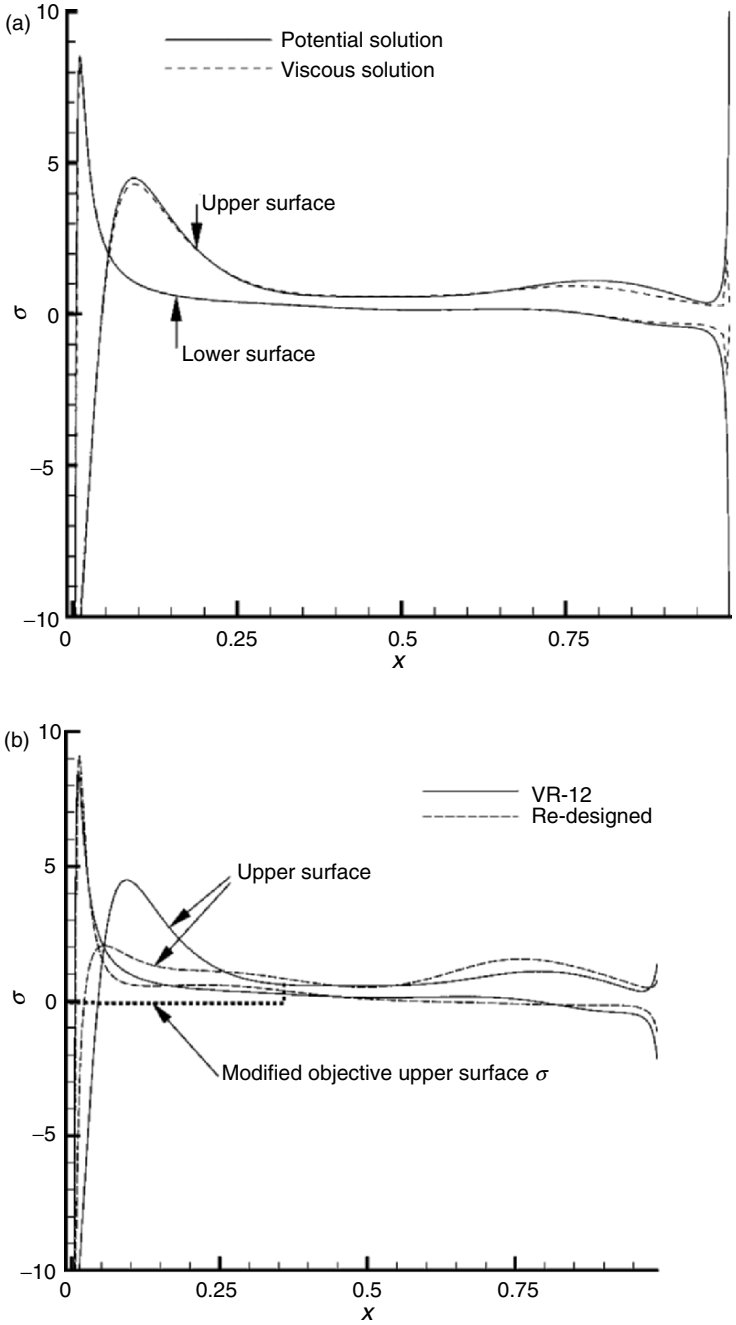


**Fig. 11.11.** Boundary vorticity flux distributions on VR-12 airfoil (**a**) and a re-designed airfoil (**b**). The design scheme sets a projective boundary vorticity flux only in the marked local region. From Zhu (2000)

major net contributor to the total lift is the primary negative $\sigma$-peak in a very narrow region on the upper surface, right downstream of the front stagnation point. But the effect of the following positive $\sigma$-peak associated with an adverse pressure gradient is unfavorable. Suppressing this front positive peak should lead to an even better performance. By (11.55), this suppression may also cause a favorable positive rear boundary vorticity-flux peak on the upper surface.

This conjecture has been confirmed by Zhu (2000) using a simple optimal design scheme, where the objective function includes minimizing the unfavorable $\sigma$ in a front-upper region. Some airfoils with better $\sigma$-distributions were produced thereby, of which one is shown in Fig. 11.11b associated with larger stall angle and maximum lift coefficient.

### 11.4.3 Wing-Body Combination Flow Diagnosis

Compared to airfoils, much less has been known on the optimal shapes of a three-dimensional wing. An interesting boundary vorticity-flux based diagnosis of a flow over a delta wing-body combination, see Fig. 11.12, has been made by Wu et al. (1999c). The flow parameters are $\alpha = 20°$, $M = 0.3$, and $Re = 1.744 \times 10^6\,\mathrm{ft}^{-1}$.

The model has an infinitely extended cylindrical afterbody, so the flow data on the body base were not available. Therefore, the body surface is open, of which the boundary is a circle $C$ of radius $a$ on the $(y, z)$-plane at the trailing edge. The line integrals in (11.46) have to be included; in the body-axis

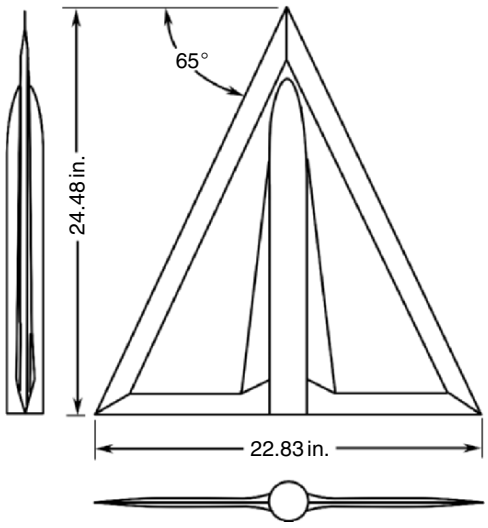


**Fig. 11.12.** A wing–body combination. From Wu et al. (1999c)

coordinate system with origin at the apex, the extended force formula gives (again ignore the skin-friction and denote $\boldsymbol{\sigma}_{\mathrm{p}}$ simply by $\boldsymbol{\sigma}$)

$$F_x = \frac{1}{2}\int_S \rho(z\sigma_y - y\sigma_z)\,\mathrm{d}S + \frac{a^2}{2}\int_0^{2\pi} p\,\mathrm{d}\theta, \tag{11.59a}$$

$$F_z = \frac{1}{2}\int_S \rho(y\sigma_x - x\sigma_y)\,\mathrm{d}S, \tag{11.59b}$$

where $S$ is the open surface of wing–body combination and $\tan\theta = z/y$. The surface integral of (11.59a) is found to provide a negative axial force (thrust), which is upset by the line integral, resulting in a net drag. The integrand $p\,\mathrm{d}\theta$ is zero except a pair of sharp positive peaks at the wing–body junctures. Thus a fairing of the junctures would reduce the drag.

On the other hand, (11.59b) traces the normal force $F_z$ to the root of the leading-edge vortices, i.e., the root of the net free vortex layers shed from the leading edges. These layers are dominated by the lower-surface boundary layer but partially cancelled by the upper-surface boundary layer. Thus, the $\boldsymbol{\sigma}$ on the upper and lower surfaces should provide a negative and positive lift, respectively. Indeed, a survey indicates that the lower-surface gives about 200% of $F_z$, but half of it is canceled by the unfavorable $\boldsymbol{\sigma}$ on the upper surface.

Moreover, it is surprising that $\boldsymbol{\sigma}$ is highly localized very near the leading edges, as demonstrated in Fig. 11.13 by the distribution of $\rho(y\sigma_x - x\sigma_y)/2$ on the contour of a cross-flow section at $x/c_0 = 0.24$, where $c_0$ is the root-chord length. The data analysis shows that an area around the leading edges, only of 1.7% of $S$, contributes to 104% of the total $F_z$. The remaining area of 98.3% $S$ merely gives $-4$% of $F_z$. This diagnosis underscores the very crucial

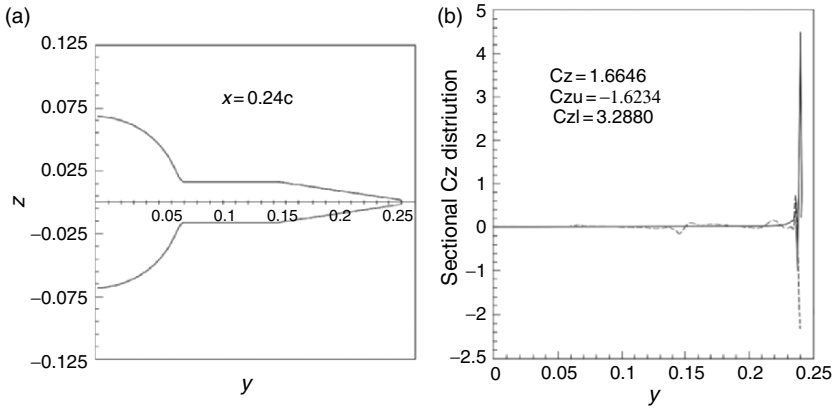


**Fig. 11.13.** (**a**) Sectional contour of the wing–body combination at $x/c_0 = 0.24$. (**b**)Boundary vorticity flux distribution. *Solid line*: lower surface, *dash line*: upper surface. From Wu et al. (1999c)

importance of near leading-edge flow management in the wing design. Should the spanwise flow on the upper surface be guided more to the $x$-direction, not only can it provide an axial momentum to reduce the drag but also the shed vortex layers from the lower surface could be less cancelled. Then stronger leading-edge vortices could be formed to give a higher normal force.

A different wing-flow diagnosis will be presented in Sect. 11.5.4.

## 11.5 A DMT-Based Arbitrary-Domain Theory

As a global view, the vorticity moment theory of Sect. 11.3 requires the data of the entire vorticity field in an externally unbounded incompressible fluid, but in flow analysis the available data are always confined in a finite and sometimes quite small domain. As an on-wall close view, boundary vorticity-flux theory of Sect. 11.4 requires only the flow information right on the body surface ("footprint" and "root" of the flow field), but is silent about how the generated vorticity forms various vortical structures that evolve, react to the body surface, and act to other downstream bodies. The shortages of these theories can be overcome by considering an *arbitrary domain* $V_f$, which has resulted in the finite-domain extensions of the above two theories, given by Noca et al. (1999) and Wu et al. (2005a), respectively.

The extension of vorticity-moment theory follows the same derivation of (11.29) from (11.27), but with all vortical terms retained at an arbitrary $\Sigma$. Like the original version, in this extension the rate of change $d/dt$ is calculated after integration is performed. The results are convenient for practical estimate of the force and moment acting to a body moving and deforming in an incompressible fluid, using measured or computed flow data. A more convenient formulation, obtained by a different DMT identity, will be given in Sect. 11.5.4. In particular, these progresses have excited significant interest in applying the new expressions to estimate the unsteady forces based on flow data measured by the particle-image velocimetry (PIV).

In contrast, the extension of the boundary vorticity-flux theory to include the flow structures in a finite $V_f$ is characterized by shifting the operator $d/dt$ into relevant integrals. This shift permits a direct generalization of the results to compressible flow, and makes it possible to quantitatively identify how each flow structure localized in both space and time affects the total force and moment, from a more fundamental point of view. The convenience of practical force estimate is not a mojor concern. This formulation is presented below. Once again we work on incompressible flow; as in Sects. 11.2 and 11.4, the compressibility effect can be easily added.

### 11.5.1 General Formulation

The formulation is based on proper derivative-moment transformation of the full expressions of $\boldsymbol{F}$ and $\boldsymbol{M}$ given by (11.1b) and (11.2b).

**Diffusion Form**

We start from identity (3.117a) for the fluid acceleration, and set $\mathcal{D} = V_\mathrm{f}$ with $\partial\mathcal{D} = \partial B + \Sigma$. Substitute this into (11.1b) and replace $\nabla \times \boldsymbol{a}$ by $\nu\nabla^2\boldsymbol{\omega}$ due to (11.5). On $\partial B$, we recognize that $\boldsymbol{n} \times \boldsymbol{a}$ is the boundary vorticity flux $\boldsymbol{\sigma}_\mathrm{a}$ due to acceleration of $\partial B$, defined in (4.24a). On $\Sigma$, we use (11.4) as well as identities (A.25) for $n = 3$ and (A.36) for $n = 2$ to transform $\boldsymbol{n} \times \boldsymbol{a}$, which makes the pressure integral in (11.1b) canceled. Therefore, we obtain (Wu and Wu 1993)

$$\boldsymbol{F} = -\frac{\mu}{k}\int_{V_\mathrm{f}} \boldsymbol{x} \times \nabla^2\boldsymbol{\omega}\,\mathrm{d}V + \boldsymbol{F}_B + \boldsymbol{F}_\Sigma, \tag{11.60}$$

where $\boldsymbol{F}_B$ and $\boldsymbol{F}_\Sigma$ are boundary integrals over $\partial B$ and $\Sigma$, respectively:

$$\boldsymbol{F}_B = \frac{1}{k}\int_{\partial B} \rho\boldsymbol{x} \times \boldsymbol{\sigma}_\mathrm{a}\,\mathrm{d}S, \tag{11.61a}$$

$$\boldsymbol{F}_\Sigma = -\frac{\mu}{k}\int_\Sigma \boldsymbol{x} \times [\boldsymbol{n} \times (\nabla \times \boldsymbol{\omega})]\,\mathrm{d}S + \mu\int_\Sigma \boldsymbol{\omega} \times \boldsymbol{n}\,\mathrm{d}S. \tag{11.61b}$$

Note that (11.61b) consists of only viscous vortical terms.

By using (A.24a), a similar approach to the moment yields

$$\boldsymbol{M} = \frac{\mu}{2}\int_{V_\mathrm{f}} x^2\nabla^2\boldsymbol{\omega}\,\mathrm{d}V + \boldsymbol{M}_B + \boldsymbol{M}_\Sigma, \tag{11.62}$$

where

$$\boldsymbol{M}_B = -\frac{1}{2}\int_{\partial B} \rho x^2\boldsymbol{\sigma}_\mathrm{a}\,\mathrm{d}S, \tag{11.63a}$$

$$\boldsymbol{M}_\Sigma = \frac{\mu}{2}\int_\Sigma x^2\boldsymbol{n} \times (\nabla \times \boldsymbol{\omega})\,\mathrm{d}S + \mu\int_\Sigma \boldsymbol{x} \times (\boldsymbol{\omega} \times \boldsymbol{n})\,\mathrm{d}S + \boldsymbol{M}_{\mathrm{s}\Sigma}, \tag{11.63b}$$

in which $\boldsymbol{M}_{\mathrm{s}\Sigma}$ is given by (11.3b).

Like $\boldsymbol{F}_B$ and $\boldsymbol{M}_B$, the integrals of $\boldsymbol{\tau}$ in $\boldsymbol{F}_\Sigma$ and $\boldsymbol{x} \times \boldsymbol{\tau}$ in $\boldsymbol{M}_\Sigma$ can be further cast to derivative-moment form as well, in terms of *vorticity diffusion flux* on a surface given by (4.23) and (4.24). Then (4.22) implies

$$-\boldsymbol{n} \times (\nabla \times \nu\boldsymbol{\omega}) = \begin{cases} \nu\boldsymbol{n} \cdot \nabla\boldsymbol{\omega} = \boldsymbol{\sigma} & \text{for } n = 2, \\ \nu\boldsymbol{n} \cdot \nabla\boldsymbol{\omega} - (\boldsymbol{n} \times \nabla) \times \nu\boldsymbol{\omega} = \boldsymbol{\sigma} - \boldsymbol{\sigma}_\mathrm{vis} & \text{for } n = 3. \end{cases} \tag{11.64}$$

Thus, for three-dimensional flow, by using (A.26) and (A.29) we obtain

$$\boldsymbol{F}_\Sigma = \frac{1}{2}\int_\Sigma \rho\boldsymbol{x} \times (\boldsymbol{\sigma} + \boldsymbol{\sigma}_\mathrm{vis})\,\mathrm{d}S, \tag{11.65}$$

$$\boldsymbol{M}_\Sigma = \frac{1}{2}\int_\Sigma \rho(2\boldsymbol{x}\boldsymbol{x} \cdot \boldsymbol{\sigma}_\mathrm{vis} - x^2\boldsymbol{\sigma})\,\mathrm{d}S + \boldsymbol{M}_{\mathrm{s}\Sigma}. \tag{11.66}$$

For flow with $Re \gg 1$, generically $|\boldsymbol{\sigma}_\mathrm{vis}| \ll |\boldsymbol{\sigma}|$.

Equations (11.60) to (11.66), characterized by the moments of $\mu\nabla^2\boldsymbol{\omega}$, can be called the *diffusion form* of the arbitrary-domain theory. It is easily seen that they hold true for compressible flow with constant $\mu$ as well. These formulas reveal explicitly the viscous root behind the classic circulation theory. The direct contribution of the body motion and deformation to the force and moment amounts to the moments of $\boldsymbol{\sigma}_a$, which is solely determined by the specified $\boldsymbol{b}(\boldsymbol{x}, t)$ and independent of the flow.

In contrast, for two-dimensional flow on the $(x, y)$-plane, apply the convention and notation defined in Sect. 11.4.1 to $\Sigma$, from (11.64) and a one-dimensional derivative-moment transformation we obtain the drag and lift components:

$$\begin{aligned} D_\Sigma &= \mu \oint_\Sigma \left( y\frac{\partial\omega}{\partial n} - x\frac{\partial\omega}{\partial s} \right) \mathrm{d}s, \\ L_\Sigma &= -\mu \oint_\Sigma \left( y\frac{\partial\omega}{\partial s} + x\frac{\partial\omega}{\partial n} \right) \mathrm{d}s, \end{aligned} \tag{11.67}$$

indicating that the local dynamics on $\Sigma$ is reflected by the *vorticity gradient vector* $\nabla\omega$. But, for $\boldsymbol{M}_\Sigma = M_\Sigma \boldsymbol{e}_z$, due to the same reason as that leading to (11.53), we stop at

$$M_\Sigma = \mu \oint_\Sigma \left( \frac{1}{2}x^2\frac{\partial\omega}{\partial n} + \boldsymbol{x}\cdot\boldsymbol{n}\omega \right) \mathrm{d}s - 2\mu\Gamma_\Sigma. \tag{11.68}$$

For flow with $Re \gg 1$, generically $|\partial\omega/\partial s| \ll |\partial\omega/\partial n|$ in (11.67) and (11.68).

### Advection Form

Owing to (11.5), $\nu\nabla^2\boldsymbol{\omega}$ in (11.60) and (11.62) can be replaced by $\nabla\times\boldsymbol{a} = \boldsymbol{\omega}_{,t} + \nabla\times\boldsymbol{l}$, where $(\cdot)_{,t} = \partial(\cdot)/\partial t$ and $\boldsymbol{l} \equiv \boldsymbol{\omega}\times\boldsymbol{u}$ is the Lamb vector. Therefore, the force and moment can be equally interpreted in terms of the local unsteadiness, advection, and stretching/tilting of the vorticity field in $V_\mathrm{f}$. But to retain the vortex force as in (11.30), we switch to identity (3.117b) that has led to the force formula (11.27). A corresponding formula for the moment can be derived from identity (A.24a). Consequently, (11.60) and (11.62) can be alternatively expressed as

$$\begin{aligned} \boldsymbol{F} = &-\rho\int_{V_\mathrm{f}} \left( \frac{1}{k}\boldsymbol{x}\times\boldsymbol{\omega}_{,t} + \boldsymbol{l} \right) \mathrm{d}V - \frac{\rho}{k}\int_{\partial V_\mathrm{f}} \boldsymbol{x}\times(\boldsymbol{n}\times\boldsymbol{l})\,\mathrm{d}S \\ &+\boldsymbol{F}_B + \boldsymbol{F}_\Sigma, \end{aligned} \tag{11.69}$$

$$\begin{aligned} \boldsymbol{M} = &\rho\int_{V_\mathrm{f}} \left( \frac{1}{2}x^2\boldsymbol{\omega}_{,t} + \boldsymbol{x}\times\boldsymbol{l} \right) \mathrm{d}V + \frac{\rho}{2}\int_{\partial V_\mathrm{f}} x^2\boldsymbol{n}\times\boldsymbol{l}\,\mathrm{d}S \\ &+\boldsymbol{M}_B + \boldsymbol{M}_\Sigma, \end{aligned} \tag{11.70}$$

where $\boldsymbol{n} \times \boldsymbol{l}$ is given by (11.28). We call this set of formulas the *advection form* of the general derivative-moment theory. The splitting of the moments of $\mu\nabla^2\boldsymbol{\omega}$ into three inviscid terms (two volume integrals and one boundary integral) further decomposes the physical mechanisms responsible for the total force and moment to their most elementary constituents. The role of the vortex force and the boundary integral of $\boldsymbol{x} \times (\boldsymbol{n} \times \boldsymbol{l})$ will be addressed in Sect. 11.5.4 for steady flow. To have a feeling on the role of $\boldsymbol{x} \times \boldsymbol{\omega}_{,t}$, consider a fish $B$ just starting to flap its caudal fin for forward motion so that $|\boldsymbol{\omega}|$ is increasing, as sketched in Fig. 11.14. Putting the other terms in (11.69) aside, based on the sign of $x$ and $y$ we can readily infer the qualitative effect of the tail swinging on the thrust and side force of the fish as indicated in the figure.

Due to the arbitrariness of the domain size, the theory can be applied to obtain the force and moment acting on any individual of a group of deformable bodies, which may perform arbitrary relative motions.

Now, as remarked earlier, as long as we use the full expression (11.69) to replace (11.27) and repeat the same steps there, a fully general version of (11.29) follows at once as the main result of the finite-domain vorticity moment theory (Noca et al. 1999). The original vorticity moment theory (J.C. Wu 1981) is then a special case of it as $\Sigma$ retreats to infinity where the fluid is at rest. On the other hand, as $\Sigma$ shrinks to the body surface $\partial B$, what remains in (11.60) and (11.62) is

$$\boldsymbol{F} = \boldsymbol{F}_B + \boldsymbol{F}_\Sigma, \quad \boldsymbol{M} = \boldsymbol{M}_B + \boldsymbol{M}_\Sigma,$$

where the normal vector $\boldsymbol{n}$ on $\Sigma$ now equals $\widehat{\boldsymbol{n}} = -\boldsymbol{n}$. Hence, substituting (11.61), (11.63), (11.65), and (11.66) into the above expressions, and using (4.23) and (4.24), we recover (11.44) and (11.45) of the boundary vorticity-flux theory for three-dimensional flow at once. The proof for two-dimensional flow is similar. A unification of various DMT-based theories is therefore achieved.

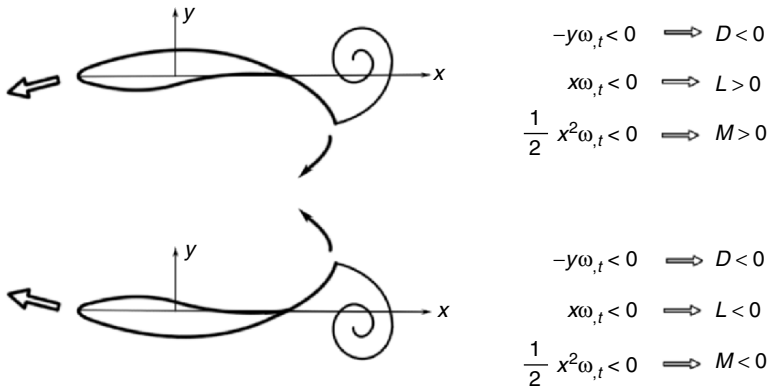


**Fig. 11.14.** A qualitative assessment of the effect of unsteady vorticity moments on the total force and moment

**The Effect of Compressibility**

By an inspection of the structure of (11.69) and (11.70) as well as a comparison of (11.4) and (11.13), we find that to generalize these formula to compressible flow it suffices to make simple replacements

$$\rho\boldsymbol{\omega}\times\boldsymbol{u}\Longrightarrow\rho\boldsymbol{\omega}\times\boldsymbol{u}-\frac{1}{2}q^2\nabla\rho,\quad \rho\boldsymbol{\omega}_{,t}\Longrightarrow\nabla\times(\rho\boldsymbol{u}_{,t}).$$

This leads to

$$\begin{aligned}\boldsymbol{F}=&-\frac{1}{k}\int_{V_\mathrm{f}}\boldsymbol{x}\times\nabla\times(\rho\boldsymbol{u}_{,t})\,\mathrm{d}V-\int_{V_\mathrm{f}}\left(\rho\boldsymbol{l}-\frac{1}{2}q^2\nabla\rho\right)\mathrm{d}V\\&-\frac{1}{k}\int_{\partial V_\mathrm{f}}\boldsymbol{x}\times\left[\boldsymbol{n}\times\left(\rho\boldsymbol{l}-\frac{1}{2}q^2\nabla\rho\right)\right]\mathrm{d}S+\boldsymbol{F}_B+\boldsymbol{F}_\Sigma,\end{aligned}\tag{11.71}$$

$$\begin{aligned}\boldsymbol{M}=&-\frac{1}{2}\int_{V_\mathrm{f}}x^2\nabla\times(\rho\boldsymbol{u}_{,t})\,\mathrm{d}V-\int_{V_\mathrm{f}}\boldsymbol{x}\times\left(\rho\boldsymbol{l}-\frac{1}{2}q^2\nabla\rho\right)\mathrm{d}V\\&+\frac{1}{2}\int_{\partial V_\mathrm{f}}x^2\boldsymbol{n}\times\left(\rho\boldsymbol{l}-\frac{1}{2}q^2\nabla\rho\right)\mathrm{d}S+\boldsymbol{M}_B+\boldsymbol{M}_\Sigma.\end{aligned}\tag{11.72}$$

The analogy between (11.71) and (11.16) is obvious. By using the numerical scheme developed by Chang and Lei (1996a) in their diagnosis of transonic viscous flow over circular cylinder based on the projection theory (Sect. 11.2.2), a similar diagnosis has been performed by Luo (2004) based on (11.71), for which $\Sigma$ can be quite small. The flow remains steady in the computed Mach-number range $M\in[0.6,1.6]$. Among Luo's results an interesting finding is that the compressing effect $-q^2\nabla\rho/2$ prevails over the vortex force $\rho\boldsymbol{\omega}\times\boldsymbol{u}$ at the same subsonic Mach number as Chang and Lei found, and that the vortex force changes from a drag to a thrust at the same supersonic Mach number as Chang and Lei found. These qualitative turning points, therefore, are independent of the specific local-dynamics theories.

### 11.5.2 Multiple Mechanisms Behind Aerodynamic Forces

In addition to the global view represented by the vorticity moment theory and the on-wall close view represented by the boundary vorticity flux theory, the present arbitrary-domain theory further enriches one's views of the physical mechanisms that have net contribution to the force and moment. How this is so has been exemplified by Wu et al. (2005a), using the unsteady two-dimensional and incompressible flow over a stationary circular cylinder of unit radius at $Re=500$ based on diameter. The flow field was solved numerically using a scheme developed by Lu (2002). An instantaneous plot of vorticity contours, in which the Kármán vortex street is clearly seen, is shown in Fig. 11.15. Since the computational domain does not cover the entire vorticity field, the figure represents a *mid-field view*.

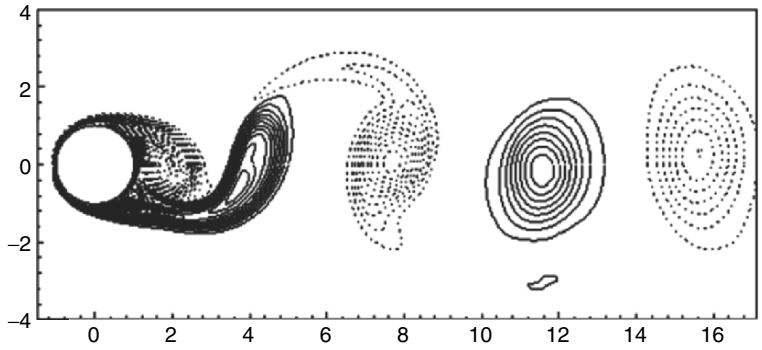


**Fig. 11.15.** An instantaneous vorticity contour (from −20 to 20 with increment 0.25) of flow over circular cylinder. In this and following figures solid and dashed lines represent positive and negative values, respectively. From Wu et al. (2005a)

It is well known that the unsteady force and moment acting to the cylinder are associated with the motion of the vortex street. However, as pointed out in Sect. 11.1, this common flow-visualization plot (along with the plots of velocity field and pressure contours, etc.,) does not tell precisely which part of each vortex in the street has a positive, negative, or zero instantaneous contribution to the total drag and lift. This information can only be found from the integrand distributions of the derivative-moment formulas (as well as those of the projection-theory of Sect. 11.2), obtained by a simple postprocessing of the flow data. Let us focus on the total drag and lift.

Take $\Sigma$ as concentric circles of varying radius $R$. In the following expressions the integrands of field integrals are expressed in Cartesian coordinates, while those in boundary integrals in polar coordinates $(r, \theta)$. Then (11.60) yields

$$\begin{aligned} D(t) &= -\mu \int_{V_\mathrm{f}} y\nabla^2\omega \,\mathrm{d}S + \mu R^2 \oint_\Sigma \left( \frac{\partial \omega}{\partial r}\sin\theta - \frac{1}{R}\frac{\partial \omega}{\partial \theta}\cos\theta \right) \mathrm{d}\theta \\ &= D_1 + D_2 + D_3, \end{aligned} \tag{11.73a}$$

$$\begin{aligned} L(t) &= \mu \int_{V_\mathrm{f}} x\nabla^2\omega \,\mathrm{d}V - \mu R^2 \oint_\Sigma \left( \frac{\partial \omega}{\partial r}\cos\theta + \frac{1}{R}\frac{\partial \omega}{\partial \theta}\sin\theta \right) \mathrm{d}\theta \\ &= L_1 + L_2 + L_3, \end{aligned} \tag{11.73b}$$

where and below $D_1, ..., L_3$ etc. denote corresponding integrals symbolically. In these formulas, by (11.69) there is

$$\begin{aligned} D_1 &= \int_{V_\mathrm{f}} \rho \left( -y\frac{\partial \omega}{\partial t} + v\omega \right) \mathrm{d}S + R \oint_\Sigma \rho\omega u_r \sin\theta \,\mathrm{d}\theta \\ &= D_4 + D_5 + D_6, \end{aligned} \tag{11.74a}$$

$$\begin{aligned} L_1 &= \int_{V_\mathrm{f}} \rho \left( x\frac{\partial \omega}{\partial t} - u\omega \right) \mathrm{d}S - R \oint_\Sigma \rho\omega u_r \cos\theta \,\mathrm{d}\theta \\ &= L_4 + L_5 + L_6. \end{aligned} \tag{11.74b}$$

In particular, when $\Sigma$ shrinks to the cylinder surface at $r = 1$, (11.73) reduces to the boundary vorticity-flux formulas

$$D = (D_2 + D_3)_{r=1}, \tag{11.75a}$$

$$L = (L_2 + L_3)_{r=1}. \tag{11.75b}$$

Equations (11.73–11.75) form a set of derivative-moment formulas for the force diagnosis, each yielding a special insight into the physics responsible for $D$ and $L$. Below we look at the distributions of their integrands.

### Mid-Field View

The inviscid decompositions of $D_1$ and $L_1$ given by (11.74) are shown in Figs. 11.16 and 11.17, respectively. As a mid-field view, these plots exhibit the same vortex structures as Fig. 11.15. But, due to the sign change of $\omega_{,t}, v$ and $y$, as a vortex passes a spatial point $\boldsymbol{x}$ the contribution of a single wake vortex may be split into two or even four pieces. It is this further identification of the net effect of every piece of a vortex constitutes the additional information carried by the local dynamics of the wake field. Note that the integrand of $L_4$, i.e., the unsteady term $\rho x \omega_{,t}$, does not reduce as $x$ increases (see Fig. 11.16a). But this does not matter since in a finite domain the integral-convergence problem does not exist, while when $\Sigma$ retreats to infinity the theory becomes the vorticity-moment theory with well-behaved convergence.

### Near-Field View

Although mathematically the diffusion form (11.60) is exactly equivalent to the advection form (11.69), for a flow at large Reynolds numbers that is our main interest the flow regions where the peak integrands of these alternative forms are very different. In the well-developed wake vortices $\mu|\nabla^2\boldsymbol{\omega}|$ has become quite weak, but it is very strong in boundary layers and free shear layers, across which $\mu|\nabla^2\boldsymbol{\omega}| \simeq \mu|\boldsymbol{\omega}_{,nn}|$ reaching $O(1)$. While in the advection form one already sees highly localized wake-vortex structures, in the diffusion form the key contributors to $\boldsymbol{F}$ and $\boldsymbol{M}$ are even more compact. Consequently, for flow with $Re \gg 1$, switching from the advection form to diffusion form implies tracking the more upstream vortical structure of those shown in Fig. 11.15. An observer watching the diffusion form naturally gains a *near-field view*, as demonstrated by Fig. 11.18 that shows the field of the integrand of $D_1$ and $L_1$.

It is remarkable that, as a sharp contrast to Figs. 11.16 and 11.17, according to (11.73) the near-field boundary layers and separated shear layers right before the formation of the Kármán vortex street have about 90% of the net contribution to $D$ and $L$. Each free vortex layer exhibits a sandwich structure because across such a layer $\omega_{,nn}$ changes sign twice. Once a concentrated wake vortex is formed and sheds downstream with its feeding sheet being cut off, it joins the rows of wake vortices which as a whole have only about 10% direct contribution to the forces.

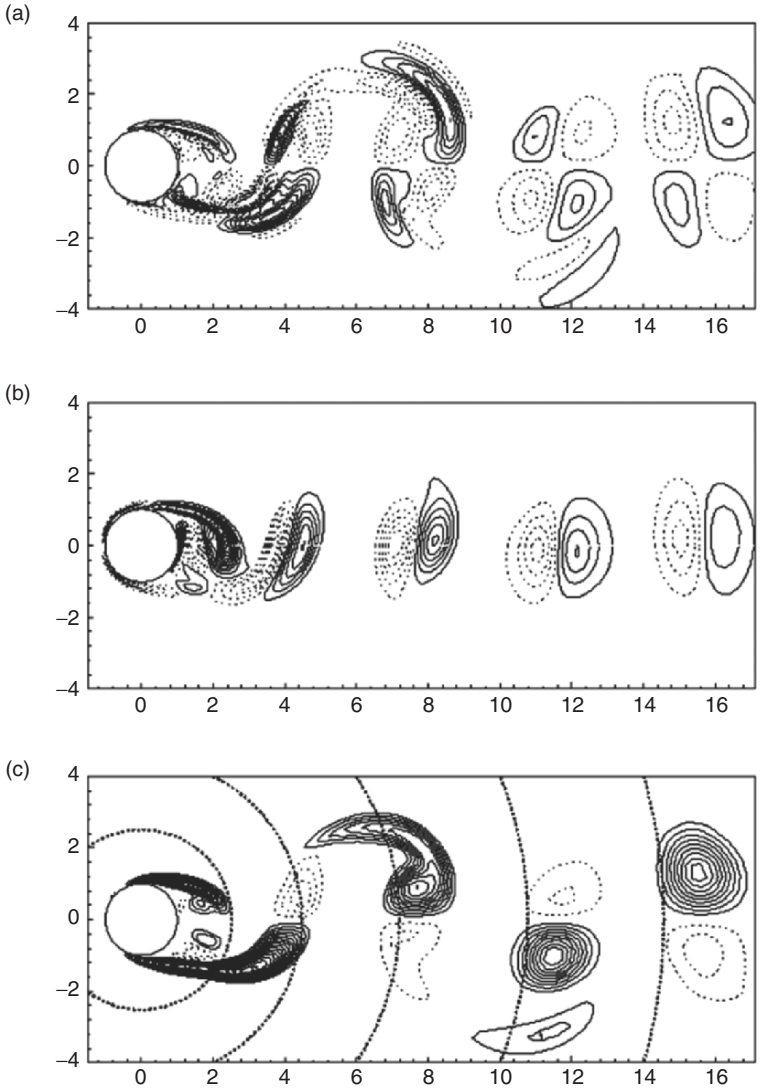


**Fig. 11.16.** Distribution of integrand of (**a**) $D_4$ from $-5$ to 5 with increment 0.5; (**b**) $D_5$ from $-5$ to 5 with increment 0.25; and (**c**) $D_6$ from $-2$ to 6 with increment 0.2. The $\theta$-variation of the integrand of $D_6$ depends on $R$, which can be qualitatively read off in (c) from the intersections of the field distribution and a few concentric circles. From Wu et al. (2005a)

The vortices in the vortex street are all product of the rolling-up of these separated shear layers, and Fig. 11.18 convincingly indicates that (11.60) can indeed trace the key local dynamic structures for the total force toward their

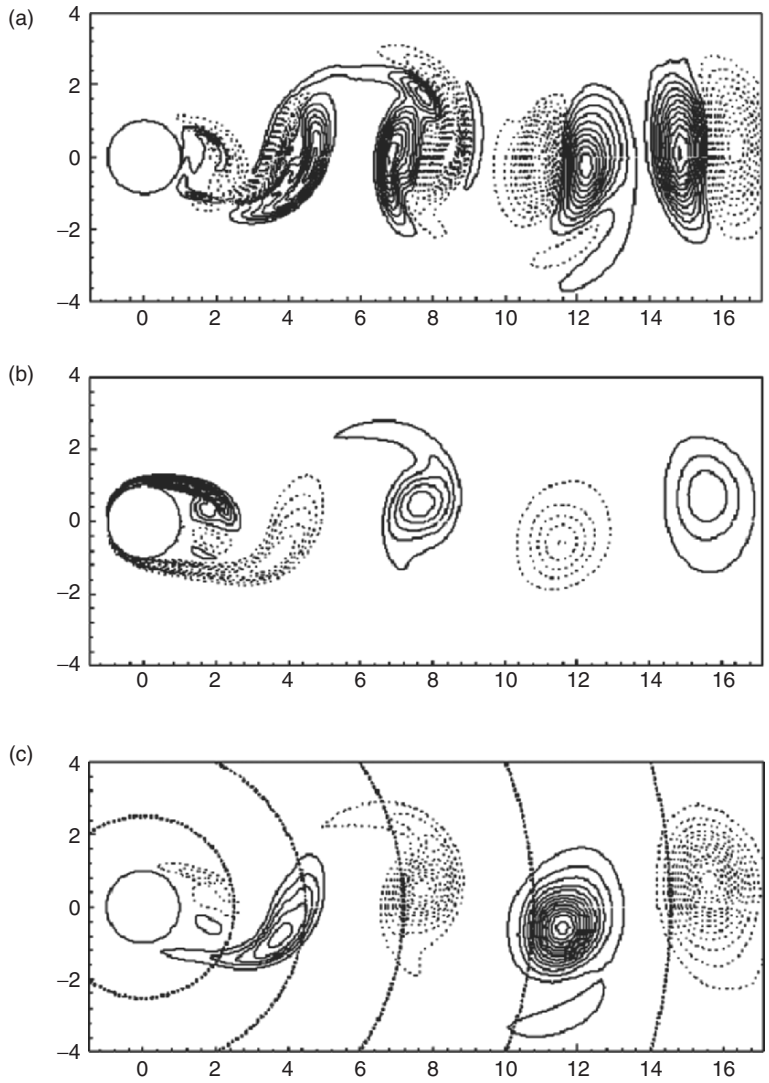


**Fig. 11.17.** Distribution of integrand of (**a**) $L_4$ from $-25$ to 25 with increment 0.5; (**b**) $L_5$ from $-10$ to 10 with increment 0.5; and (**c**) $L_6$ from $-40$ to 40 with increment 2. The $\theta$-variation of the integrand of $L_6$ can be qualitatively read off similar to Fig. 11.16c. From Wu et al. (2005a)

origin, a task that cannot be achieved by standard formulas. Of course, the Kármán street does strongly influence the total force; but its major effect is indirect through its induced unsteadiness of the flow, including the periodic swing of the peak $\nabla^2\omega$ in near-field vortex layers.

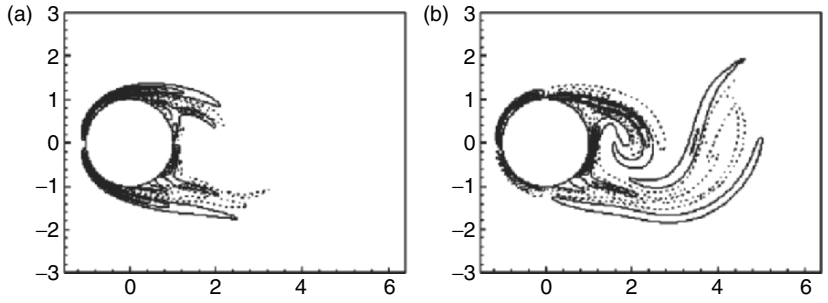


**Fig. 11.18.** Distribution of integrand of (**a**) $D_1$ and (**b**) $L_1$. Contours from $-10$ to 10 with increment 0.5. From Wu et al. (2005a)

### On-Wall Close View

If the radius of $\Sigma$ is $R_0 = 1 + \delta$ with $\delta \ll 1$ such that $V_\mathrm{f}$ is well within the sublayer of the boundary layer adjacent to the cylinder and the flow therein is dominated by diffusion, then $\boldsymbol{F}_\Sigma$ contributes to almost all $\boldsymbol{F}$ and the Stokes approximation (Sect. 4.2.1) can be applied in a way very similar to that discussed in Sect. 11.4.1. The result is actually independent of $R_0$ and equal to that obtained by (11.75) since the radius is canceled during integration. Therefore, to the above physical pictures we may add Fig. 11.19, which shows the $\theta$-variation of the two terms in (11.75a,b) as the on-wall close view. Recall that the normal and tangent components of $\nabla\omega$ are from respectively the pressure gradient ($\sigma = \sigma_\mathrm{p}$) and skin-friction, and the former is much stronger than the latter, it is still the moments of $\sigma$ that dominate the drag and lift. We have seen in the context of Fig. 4.12 that the sign change of $\sigma_\mathrm{p}$ signifies that the boundary layer is about to separate; now $x = \cos\theta$ and $y = \sin\theta$ in (11.75) add additional sign changes of the integrand in $D$ and $L$, resulting in their different $\theta$-dependence.

Notice the physical relation between Figs. 11.18 and 11.19. The boundary layers and their separation in the former are the *spatial and temporal accumulated effect* of the boundary vorticity fluxes in the latter (Sect. 4.2.3). This could be clearly seen by comparing a time sequence of both kinds of figures.

The above discussions have shown how different views capture different stages of the evolution of the same vorticity field, and how the physics of these stages are consistent and complementary to each other. Taking together, they form a complete multidimensional picture of the mechanisms responsible for the force and moment.

It should be stressed that a vortical structure favorable to the force and moment at one of its evolution stage may become unfavorable at another stage, although in terms of the flow data at any stage one can always infer the same force and moment. Therefore, as yet another *evolution view*, one may trace the motion of each individual structure (or a group of structures),

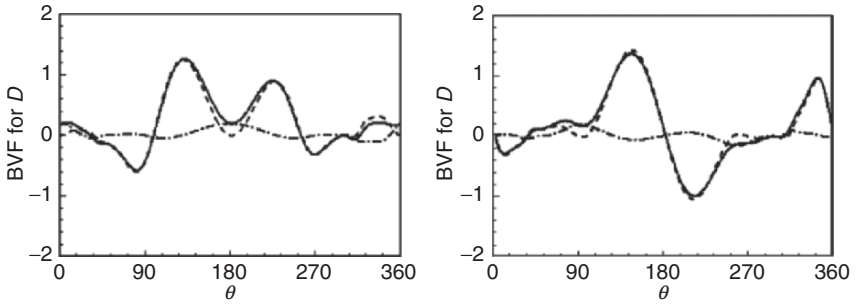


**Fig. 11.19.** Distributions of the integrands of (**a**) drag and (**b**) lift for the moments of vorticity-gradient components on the cylinder surface, see (11.75). *Solid lines*: total force, *dashed lines*: contribution of $\mu\partial\omega/\partial r$, *dashed–dot lines*: contribution of $\mu\partial\omega/\partial s$. From Wu et al. (2005a)

observing its "role switch," and assess its merit. Such a thorough quantitative assessment would be very beneficial in creating new configurations and flow-control strategy.

### 11.5.3 Vortex Force and Wake Integrals in Steady Flow

We now return to classic aerodynamics on steady flow over a stationary rigid body. Assume the Reynolds number is sufficiently large, all the attached boundary layers of the body are enclosed by $\Sigma$ which only cuts vortical flow in the wake. The preceding example of circular-cylinder flow has indicated that in the fully developed wake region the viscous vorticity gradient is much smaller than $O(1)$. This is generally true in high Reynolds-number steady aerodynamics, and right on $\Sigma$ one can neglect the effect of $\mu\nabla\boldsymbol{\omega}$ compared to the pressure force; namely, the entire $\boldsymbol{F}_\Sigma$ and $\boldsymbol{M}_\Sigma$ in (11.69) and (11.70) can be dropped.[11] Therefore, since $\boldsymbol{F}_B$ and $\boldsymbol{M}_B$ also vanish, we simply have

$$\boldsymbol{F} = -\rho\int_{V_\mathrm{f}} \boldsymbol{l}\,\mathrm{d}V - \frac{\rho}{k}\int_\Sigma \boldsymbol{x}\times(\boldsymbol{n}\times\boldsymbol{l})\,\mathrm{d}S \tag{11.76a}$$

$$= -\frac{\rho}{k}\int_{V_\mathrm{f}} \boldsymbol{x}\times(\nabla\times\boldsymbol{l})\,\mathrm{d}V = -\frac{\mu}{k}\int_{V_\mathrm{f}} \boldsymbol{x}\times\nabla^2\boldsymbol{\omega}\,\mathrm{d}V, \tag{11.76b}$$

$$\boldsymbol{M} = -\rho\int_{V_\mathrm{f}} \boldsymbol{x}\times\boldsymbol{l}\,\mathrm{d}V + \frac{\rho}{2}\int_\Sigma x^2\boldsymbol{n}\times\boldsymbol{l}\,\mathrm{d}S \tag{11.77a}$$

$$= \frac{\rho}{2}\int_{V_f} x^2\nabla\times\boldsymbol{l}\,\mathrm{d}V = \frac{\mu}{2}\int_{V_\mathrm{f}} x^2\nabla^2\boldsymbol{\omega}\,\mathrm{d}V. \tag{11.77b}$$

[11] This does not imply the neglect of viscosity inside $V_\mathrm{f}$. It is the accumulated effect of the viscous force in $V_\mathrm{f}$ that forms the dominant feature of the wake.

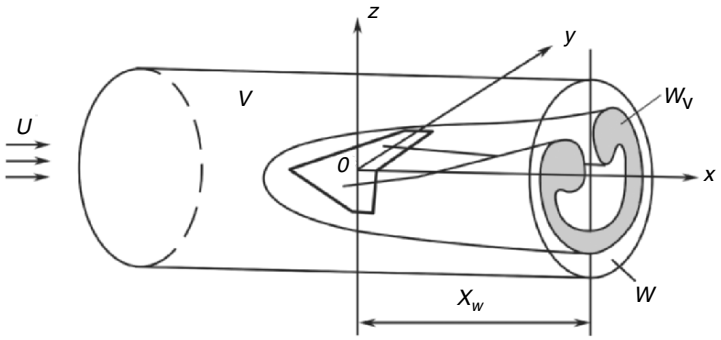


**Fig. 11.20.** Control volume $V$ in which the flow is steady, wake plane $W$, and its vortical part $W_\mathrm{v}$. From Wu and Wu (1996)

Therefore, *for steady flow at large Re, no transverse Lamb vector, no force and moment.*

Let us concentrate on the force given by (11.76) and consider a wing flow schematically drawn in Fig. 11.20. The oncoming flow has uniform velocity $\boldsymbol{U} = U\boldsymbol{e}_x$ in the wind-axis coordinate system $(x, y, z)$. The flow in a cylindrical control volume $V$ is assumed steady and symmetric with respect to the $(x, z)$-plane. $V$ has sufficiently remote side boundary $S$ and a downstream boundary $W$ on the $(y, z)$-plane (a *Wake plane*) at an arbitrary fixed $x$ location with $\boldsymbol{n} = \boldsymbol{e}_x$ there, such that the vorticity can be set zero over $\Sigma$ except a small vortical part of $W$, $W_\mathrm{v} \ll W$. Hence, in (11.76a) the $\Sigma$-integral reduces to a $W_\mathrm{v}$-integral.

One's concern in the flow property on a wake-plane is mainly from experimental aerodynamics. It has long been hoped that for steady flow a wake-plane survey may permit inferring the lift and drag on the body as an alternative to the balance measurement and the very difficult measurement of body-surface skin friction. For example, the approximate lift formula (11.38) has been used for decades. In what follows we use (11.76a) to address three problems of considerable practical interest. We denote

$$\boldsymbol{u} = (U + u', v, w), \quad p = p_\infty + p'. \tag{11.78}$$

### On the Distinction of Induced and Profile Drags

In steady flow, the drag consists of induced drag (see (11.7b)) and *profile drag.* The latter is associated with the shedding of low-energy viscous boundary-layer flow into the wake. Unlike the lift and induced drag which exist even in the Euler limit ($Re \to \infty$), the profile drag appears only at finite $Re$. How to rationally distinct the two drag constituents for a general nonlinear and viscous flow is important, since to alleviate them one has to use different methods based on their respective physical roots (cf. Kroo 2001).

Consider the Euler limit first, where the vortex-sheet Lamb vector (Sects. 4.4.1 and 11.3.3) in steady flow is nonzero only in the "bound vortex," i.e., the boundary layers attached to the wing. Thus, in (11.76a) the $W_\mathrm{v}$-integral disappears, and we see at once that the vortex force must be the only source of both lift and induced drag:

$$L = -\rho \int_V l_x \,\mathrm{d}V = \rho \int_V (u\omega_y - v\omega_x)\,\mathrm{d}V, \tag{11.79a}$$

$$D_\mathrm{in} = -\rho \int_V l_y \,\mathrm{d}V = \rho \int_V (v\omega_z - w\omega_y)\,\mathrm{d}V. \tag{11.79b}$$

In fact, from these formulas one may easily deduce (11.7a) and (11.7b) as linearized approximation.

We can also recover (11.38) from the vortex force, by using (A.22):

$$-\rho \int_{V_\mathrm{f}} \boldsymbol{l}\,\mathrm{d}V \simeq \rho \boldsymbol{U} \times \int_{V_\mathrm{f}} \boldsymbol{\omega}\,\mathrm{d}V = \rho U \boldsymbol{e}_z \int_{W_\mathrm{v}} y\omega_x \,\mathrm{d}S. \tag{11.80}$$

Note that, as a mid-field view, here the relevant vortex dynamics mechanism is more upstream than that in deriving (11.38) based on the global view. While in the latter we focused on the increase of the vortex-loop area, now we are focusing on the vorticity inside the wing boundary layers. This is evident in two-dimensional flow, for which (11.5) directly follows from (11.79b) without appealing to the starting vortex.

The induced drag can also be approximately expressed by a wake-plane integral. Similar to the derivation of (11.7a) from (11.38), by (11.9) and the same one-dimensional derivative-moment transformation for $\Gamma$ used there, since the integral of $wd(y\Gamma)/dy$ vanishes due to the symmetry, (11.7b) is cast to (Wu et al. 2002)

$$D_\mathrm{in} = -\rho \int_{-s}^{s} yw(y)\gamma(y)\,\mathrm{d}y, \tag{11.81a}$$

which is the vortex-sheet form of a more general wake integral for distributed vorticity, in pair with (11.38):

$$D_\mathrm{in} \simeq -\rho \int_{W_\mathrm{v}} yw\omega_x \,\mathrm{d}S. \tag{11.81b}$$

We now turn to the finite-$Re$ effect reflected by the boundary integral of (11.76), which is a wake integral of

$$\boldsymbol{x} \times (\boldsymbol{n} \times \boldsymbol{l}) = \boldsymbol{e}_x(\boldsymbol{x} \cdot \boldsymbol{l}) - x\boldsymbol{l} = \boldsymbol{e}_x(\boldsymbol{x}_\pi \cdot \boldsymbol{l}) - x\boldsymbol{l}_\pi,$$

where the suffix $\pi$ denotes the $(y, z)$ components tangent to $W$. On $W$ the Lamb vector can be replaced by the total-pressure gradient due to the steady Crocco equation

$$\rho\boldsymbol{\omega} \times \boldsymbol{u} = -\nabla P, \quad P \equiv p + \frac{1}{2}\rho q^2, \tag{11.82}$$

of which both sides approach zero simultaneously in the Euler limit. Since $x = x_w$ is fixed and $\nabla P = \nabla P'$ where $P' = P - P_\infty$ vanishes at $\partial W$, the integral of $\rho x \boldsymbol{l}_\pi = -x\nabla_\pi P'$ over $W$ vanishes. Thus, the wake integral yields a drag only, which is the profile drag:

$$D_{\text{prof}} = -\frac{\rho}{k}\boldsymbol{e}_x \int_{W_\text{v}} \boldsymbol{x}_\pi \cdot \boldsymbol{l}\, \mathrm{d}S \tag{11.83a}$$

$$= -\boldsymbol{e}_x \int_{W_\text{v}} P'\, \mathrm{d}S. \tag{11.83b}$$

Equation (11.83b) is the exact formula for deducing the profile drag from the measured total-pressure deficit over $W_\text{v}$. Its vorticity-dynamics origin is revealed by (11.83a): the nonBeltramian behavior of the viscous flow at finite $Re$. To see relevant mechanisms explicitly, denote the Euler-limit values of $\boldsymbol{l}$, $\boldsymbol{\omega}$, and $\boldsymbol{u}$ by suffix 0 and their residual values at finite $Re$ by a tilde, so that

$$\tilde{\boldsymbol{l}} = \boldsymbol{\omega}_0 \times \tilde{\boldsymbol{u}} + \tilde{\boldsymbol{\omega}} \times \boldsymbol{u}_0 + \tilde{\boldsymbol{\omega}} \times \tilde{\boldsymbol{u}}.$$

we may then replace $\boldsymbol{l}$ in (11.83a) by $\tilde{\boldsymbol{l}}$, and find a leading-order cause of the profile drag

$$D_{\text{prof}} \simeq \frac{\rho}{k} U \int_{W_\text{v}} (z\tilde{\omega}_y - y\tilde{\omega}_z)\, \mathrm{d}S. \tag{11.84}$$

As shown in Fig. 11.21, the wing boundary layers from upper and lower surfaces have positive and negative $\tilde{\omega}_y$, respectively, which merge at the trailing edge and form a wake of finite thickness, with $z\tilde{\omega}_y > 0$. This is the entire $D_{\text{prof}}$ in two dimensions. In three dimensions the side edges of the wing also have boundary layers, which yields $-y\tilde{\omega}_z > 0$ at both sides.

### On the Forces by Vortical-Wake Integrals

It has been highly desired to express, if possible, the forces by integrals only over the vortical part of the wake plane, $W_\text{v} \ll W$, because the entire $W$ is

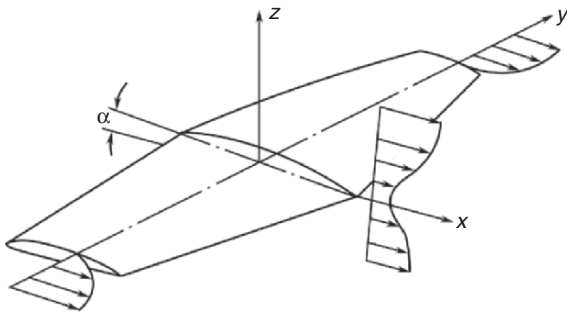


**Fig. 11.21.** Viscous sources of profile drag according to (11.84)

often too large to make a velocity survey. We have just seen that the profile-drag formula satisfies this need. To see to what extent the lift and induced drag can be likewise expressed, we first notice that the vortex force can be cast to an integral over a full $W$. By using the mass conservation one has the balance of momentum-flux through $W$ and side boundary $S$ (Batchelor 1967):

$$\int_S \boldsymbol{u} u_n \,\mathrm{d}S = -\boldsymbol{e}_x \int_W U u' \,\mathrm{d}S,$$

by which and identity (3.69) one transforms (11.79) to (Yates and Donaldson 1986)

$$L = -\int_W uw \,\mathrm{d}S, \quad D_{\mathrm{in}} = \frac{1}{2}\int_W (q_\pi^2 - u'^2)\,\mathrm{d}S, \tag{11.85}$$

where $q_\pi^2 = v^2 + w^2$. Note in passing that substituting these and (11.83) into (11.76), we recover the conventional wake integrals for lift and drag, which are a component form of (2.74) and have been the standard starting point of flow diagnosis by experimentally measured wake data:

$$L = -\rho \int_W uw \,\mathrm{d}S, \tag{11.86a}$$

$$D = \int_W [(p_\infty - p) + u(U-u)]\,\mathrm{d}S. \tag{11.86b}$$

However, (11.85) no longer has vortical form nor exhibits local dynamics. Unfortunately, there is no other way but the kinematic identity (3.69) to cast the Lamb-vector volume integral to boundary integral. Therefore, in exact form one has to be satisfied with either the compact vortical form (11.76) but allowing for volume integral, or wake integrals (11.85) over a large $W$. In other words, *it is impossible to exactly express the lift and induced drag by any wake integrals over the vortical region only.*

Nevertheless, some approximate formulas solely in terms of integrals over $W_{\mathrm{v}}$ are available. For the induced drag, so far the best result is the leading-order approximation (11.81b). For the lift, the best result follows from transforming (11.86b) by identity (A.26) (Wu and Wu 1989):

$$L = \rho \int_{W_{\mathrm{v}}} y[u\omega_x - (v\omega_y + w\omega_z)]\,\mathrm{d}S + \rho \int_W (wv_{,x} - vw_{,x})\,\mathrm{d}S, \tag{11.87}$$

of which the leading order is (11.80) or again (11.38). The second integral in (11.87) represents a small near-field correction to ensure the lift is independent of $x$, of which the integrand is not confined to $W_{\mathrm{v}}$.

Equation (11.87) has been applied to the diagnosis of a steady incompressible flow over a delta wing with leading-edge vortices, based on the measured data over a wake plane near the trailing edge (Wu et al. 1996).[12]

[12] In Wu and Wu (1989) and Wu et al. (1996) the drag formula is in error.

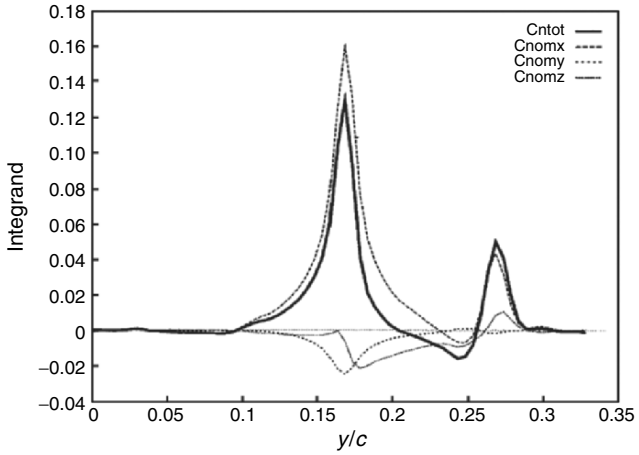


**Fig. 11.22.** Spanwise distribution of normal force and its vortical constituents over a half delta wing. From Wu et al. (1996)

The wing has sharp leading edge of 76° sweeping angle, and is at $\alpha = 20°$ and $Re = 1.14 \times 10^6\,\mathrm{ft}^{-1}$. With coordinates fixed to the wing, the wake plane $W$ is at $x/c = 0.075$ downstream of the trailing edge, on which a set of measured data of $(u, v, w, p, P)$ for half wing was utilized to infer the three vorticity components. The data show a strong leading-edge vortex, of which the core axial velocity is as high as $u = 1.8U$. This is the key structure of producing the normal force along with a negative axial force.

Figure 11.22 shows the spanwise normal load distribution from wing centerline to wing tip (integration along $z$ has been performed) computed from (11.87). Also shown are separate contributions from $\omega_x$, $\omega_y$, and $\omega_z$ in its $W_\mathrm{v}$-integral. The vortical wake integral of $yu\omega_x$ is dominant, leading to a local peak of lift/drag ratio of order 10 at the leading-edge vortex location. A weaker peak of normal load appears outside the wing tip, which is the place where boundary layers (dominated by that from the lower surface) leave the wing, with very low total pressure and hence a large axial force. The local $C_\mathrm{l}/C_\mathrm{d}$ there is only of order one. Therefore, a better aerodynamic performance would be gained if the wing tip is properly cut off, as in many successful wing designs.

### Forces in Terms of Flow Data Downstream of a Wake Plane

There are occasions where the flow-field survey can hardly be done around the body, and what one can measure is only a downstream wake. Hence, it is of interest to see whether an observer sitting in such the wake, without seeing the flow around body at all, can still infer exactly the same $\boldsymbol{F}$ as (11.86). We show that the answer is positive.

Use a wake plane $W$ to cut the whole space $V_\infty$ into a "front" and a "rear" control volumes, $V$ and $R$, respectively, see Fig. 11.23. Conceive that

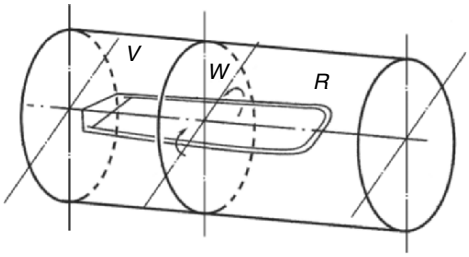


**Fig. 11.23.** The "front" and "rear" control volumes $V$ and $R$ divided by a wake plane $W$, with $V + R = V_\infty$

a front observer $A$ and a rear observer $B$ can only see the flows in $V$ and $R$, respectively. Kinematically, the two observers are linked by relations

$$\int_V \boldsymbol{\omega}\,\mathrm{d}V = \int_{W_\mathrm{v}} \omega_x \boldsymbol{x}\,\mathrm{d}S, \quad \int_{W_\mathrm{v}} \omega_x\,\mathrm{d}S = 0, \tag{11.88}$$

$$\int_R \boldsymbol{l}(\boldsymbol{x},t)\,\mathrm{d}V = -\int_V \boldsymbol{l}(\boldsymbol{x})\,\mathrm{d}V. \tag{11.89}$$

Dynamically, their bridge can be found from the vorticity-moment formula (11.48), by which it easily follows that

$$\boldsymbol{F} = -\rho\left(\frac{\mathrm{d}\boldsymbol{I}_V}{\mathrm{d}t} + \frac{\mathrm{d}\boldsymbol{I}_R}{\mathrm{d}t}\right) = -\rho\frac{\partial \boldsymbol{I}_R}{\partial t}. \tag{11.90}$$

Shifting $\partial/\partial t$ into the integral over $R$ and using (A.23) to manipulate the result, since viscous terms are dropped on $W$, (11.90) becomes

$$\boldsymbol{F} = \rho\int_R \boldsymbol{l}\,\mathrm{d}V + \frac{\rho}{2}\int_{W_\mathrm{v}} \boldsymbol{x}\times(\widehat{\boldsymbol{n}}\times\boldsymbol{l})\,\mathrm{d}S, \quad \widehat{\boldsymbol{n}} = -\boldsymbol{e}_x, \tag{11.91}$$

which is evidently nothing but (11.76) due to (11.89). Physically, the rear observer sees that at the upstream end of $R$ there comes a vortex pair satisfying (11.88), carrying a flux of vorticity moment into $R$ through $W_\mathrm{v}$ via the second term of (11.91). This vortex pair is connected to the starting-vortex system to form an unsteady horseshoe vortex, and the area spanned by the vortex (cut by $W_\mathrm{v}$) is increasing as shown by (11.90), which implies the vortex force in (11.91).

### 11.5.4 Further Applications

Before closing this section, we present two more applications of the derivative-moment transformation. We first extend our discussion on experiment-oriented force formulas to unsteady flow. We have seen that to obtain exact lift and drag in steady flow, the minimum requirement is to survey at least a large area of a wake plane where $\boldsymbol{u}' \neq \boldsymbol{0}$. The question now is what is the corresponding

minimum requirement if the flow around the body is *unsteady*. Experimental survey on a wake plane is certainly insufficient since the flow unsteadiness propagates to all directions. Thus we go to the next: How about on a control surface enclosing the body?

It has been believed that the answer is negative due to the extra volume integral of $\partial \boldsymbol{u}/\partial t$. Moreover, even if one can make the flow survey in a finite domain rather than merely on a wake plane, the gathered data may still be unable to fulfill the entire $V_{\mathrm{f}}$. For example, PIV can hardly detect the velocity distribution adjacent to the body surface.

Contrary to the conventional idea, however, we now show that the force formula by control-surface integral alone can be easily found once we enter the DMT-based formulation, as first shown by Noca et al. (1999). Here we follow Wu et al. (2005d), starting from (11.1c). When the flow is *incompressible*, an application of (A.22) to its first term immediately yields the desired result:

$$\boldsymbol{F} = -\rho \frac{\mathrm{d}}{\mathrm{d}t} \left( \int_{\partial B} \boldsymbol{x} b_n \, \mathrm{d}S + \int_{\Sigma} \boldsymbol{x} u_n \, \mathrm{d}S \right) - \int_{\Sigma} [p\boldsymbol{n} + \rho \boldsymbol{u}(u_n - v_n) - \boldsymbol{\tau}] \, \mathrm{d}S. \quad (11.92)$$

Alternatively, by (A.25) and (11.4) we have

$$-\int_{\Sigma} p\boldsymbol{n} \, \mathrm{d}S = -\frac{\rho}{k} \int_{\Sigma} \boldsymbol{x} \times (\boldsymbol{n} \times \boldsymbol{a}) \, \mathrm{d}S - \frac{\mu}{k} \int_{\Sigma} \boldsymbol{x} \times [\boldsymbol{n} \times (\nabla \times \boldsymbol{\omega})] \, \mathrm{d}S,$$

where the second term and the integral of $\boldsymbol{\tau}$ in (11.92) just combine to form $\boldsymbol{F}_{\Sigma}$ given by (11.65) or (11.67). Therefore, the involvement of pressure can be replaced by that of acceleration:

$$\boldsymbol{F} = -\rho \frac{\mathrm{d}}{\mathrm{d}t} \left( \int_{\partial B} \boldsymbol{x} b_n \, \mathrm{d}S + \int_{\Sigma} \boldsymbol{x} u_n \, \mathrm{d}S \right) - \frac{\rho}{k} \int_{\Sigma} \boldsymbol{x} \times (\boldsymbol{n} \times \boldsymbol{a}) \, \mathrm{d}S + \boldsymbol{F}_{\Sigma}. \quad (11.93)$$

For a specified body motion, since the PIV can yield the material acceleration $\boldsymbol{a}$ (e.g., La Porta et al. 2001; Christensen and Adrian 2002) on $\Sigma$, by which the pressure can be inferred (e.g., Liu and Katz 2004), the unsteady force can be deduced from (11.92) or (11.93).

Unfortunately, for the total moment a formula corresponding to (11.92) does not exist, since $\boldsymbol{x} \times \boldsymbol{u}$ is not divergence-free even for incompressible flow.

Equations (11.92) and (11.93) have been verified by numerical tests. One example is a two-dimensional uniform oncoming flow $\boldsymbol{U} = U\boldsymbol{e}_x$ past a *deformable* airfoil at $Re = 10^4$, of which the centerline oscillates as a traveling wave

$$y = a(x) \sin[2\pi(x - ct)], \quad (11.94)$$

where the amplitude $a(x)$ is a parabolic curve. The deformable airfoil is shown in Fig. 11.24, along with three different deformable control surfaces. Figure 11.25 is an instantaneous vorticity contour plot at phase speed $c/U = 0.5$,

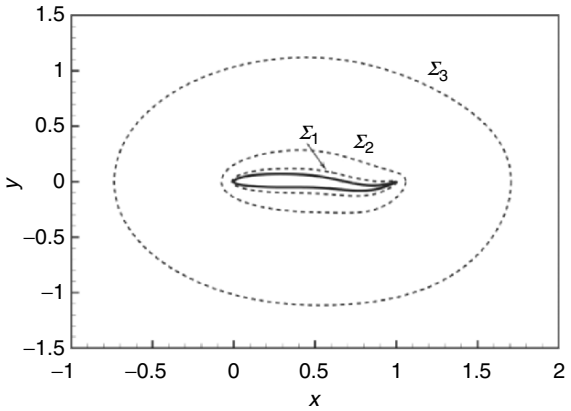


**Fig. 11.24.** A flexible airfoil with centerline defined by (11.94). Airfoil shape and three selected deformable control surfaces $\Sigma_i,\ i = 1,2,3$. From Wu et al. (2005d)

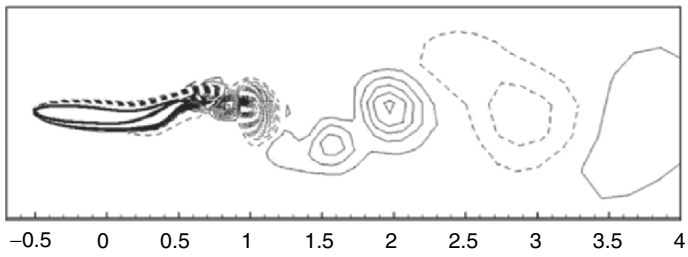


**Fig. 11.25.** An instantaneous vorticity contour plot for $c/U = 0.5$. Courtesy of Lu

and in Fig. 11.26 we plot the varying drag and lift computed by (11.92) and (11.93) over a period for the three $\Sigma$-locations at this phase speed. For comparison the result computed by (11.1a) is also shown. This example confirms the correctness of the derivative-moment formulas and the $\Sigma$-independent of of the results. The drag will become a thrust when $c/U > 1$ (not shown).

The second example is a local-dynamics diagnosis of the internal incompressible flow in a turbofan compressor, where the performance is no longer characterized by force and moment but the derivative-moment transformation can still be applied. After passing a row of rotor blades of angular velocity $\Omega$ about the $z$-axis, the fluid gains pressure and is slowed down at the exit. We analyze the flow in a domain $V$ consisting of a passage between two neighboring blades. Let the inlet plane at $z = z_0$ and exit wake plane at $z = z_1$ be perpendicular to the $z$-axis, and denoted by $S_0$ and $S_1$, respectively. Then a key stationary performance parameter is the *total-pressure ratio*, which should be as high as possible:

$$\beta \equiv \frac{1}{S_1 P_\infty} \int_{S_1} \overline{P}\, \mathrm{d}S, \quad P \equiv p + \frac{1}{2}\rho q^2, \tag{11.95}$$

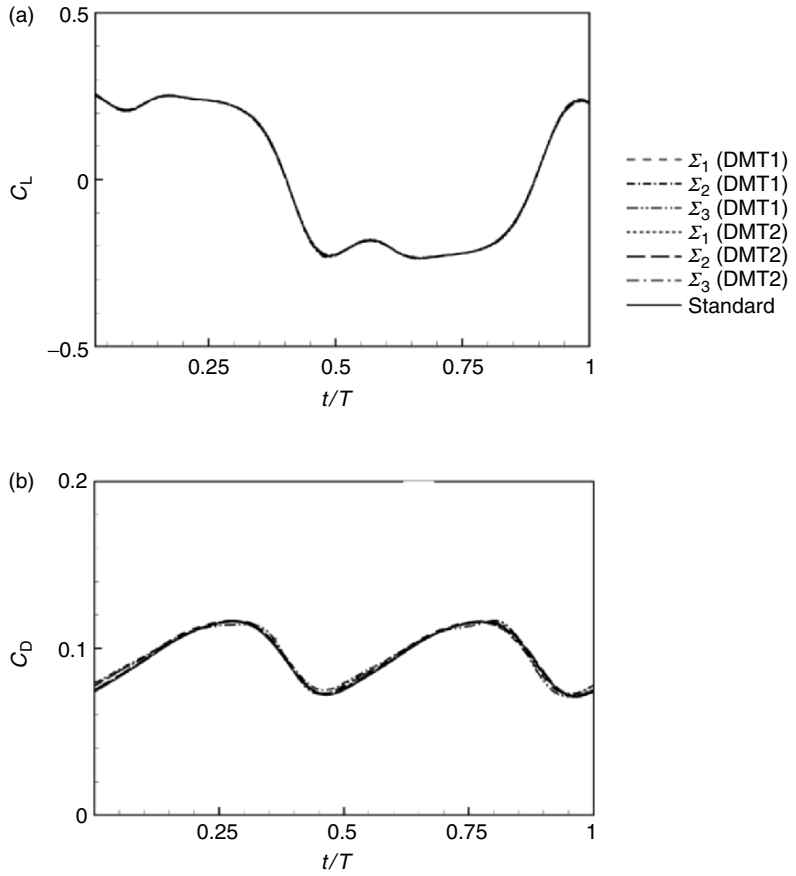


**Fig. 11.26.** The time history of drag and lift coefficients of the flexible airfoil for $c/U = 0.5$, computed by (11.1a), (11.92), and (11.93) for three deformable $\Sigma_i$, $i = 1, 2, 3$. The curves computed by these formulas are marked by standard, DMT1, and DMT2, respectively. From Wu et al. (2005d)

where $q = |\boldsymbol{u}|$ and the overline denotes the time average over a cycle. Another stationary performance parameter is the compressor *efficiency* $\eta$, which we define based on (2.76):

$$\eta \equiv \frac{1}{\Omega \overline{M}_z} \left( \int_{S_1} \overline{Pu}_z \, \mathrm{d}S - P_\infty U S_0 \right), \tag{11.96}$$

where $M_z$ is the moment acting to the flow by the rotating blade. Since on both the solid blade/hub surface and the exit plane $S_1$ the work rate done by pressure force is much larger than that done by viscous stress, the latter is neglected. $Pu_z$ represents the *total-pressure flux* entering into the combustor.

Now, to find the local flow structures that influence the total-pressure radio $\beta$, we use cylindrical coordinates $(r, \theta, z)$ and write $\mathrm{d}S = r\,\mathrm{d}r\,\mathrm{d}\theta$ in (11.95). Since for any function $f(r, \theta, z, t)$ there is

$$fr = \frac{1}{2}\frac{\partial}{\partial r}(fr^2) - \frac{r^2}{2}\frac{\partial f}{\partial r},$$

we can make an one-dimensional derivative-moment transformation:

$$\int_{S_1} Pr\,\mathrm{d}r\,\mathrm{d}\theta = \frac{1}{2}\left[\int_0^{2\pi}(P_\mathrm{s}R_\mathrm{s}^2 - P_\mathrm{h}R_\mathrm{h}^2)_{z_1}\,\mathrm{d}\theta - \int_{S_1} r^2\frac{\partial P}{\partial r}\,\mathrm{d}r\,\mathrm{d}\theta\right], \tag{11.97}$$

where $r = R_\mathrm{s}(z)$ and $r = R_\mathrm{h}(z)$ define the generators of the shroud and hub, respectively, and

$$P_\mathrm{s} \equiv P(R_\mathrm{s}, z_1, \theta) = p(R_\mathrm{s}, z_1, \theta), \tag{11.98a}$$

$$P_\mathrm{h} \equiv P(R_\mathrm{h}, z_1, \theta) = p(R_\mathrm{h}, z_1, \theta) + R_\mathrm{h}^2\Omega^2 \tag{11.98b}$$

due to the adherence condition. It is now evident that the local dynamics enters the last term on the right-hand side of (11.97), through the momentum equation (11.4). Hence, (11.95) is cast to

$$\beta = \frac{1}{2S_1P_\infty}\left[\int_0^{2\pi}(\overline{P}_\mathrm{s}R_\mathrm{s}^2 - \overline{P}_\mathrm{h}R_\mathrm{h}^2)_{z_1}\,\mathrm{d}\theta + \int_{S_1}\rho r(\overline{\omega_\theta u}_z - \overline{\omega_z u}_\theta)\,\mathrm{d}S\right], \tag{11.99}$$

which clearly reveals that, except the boundary line integrals, the key mechanism is the $r$-component of the Lamb vector. A similar derivative-moment transformation can be made for the integral of $Pu_z$ in determining the efficiency $\eta$, see (11.96):

$$\int_{S_1}\overline{Pu}_z\,\mathrm{d}S = \frac{1}{2}\int_{S_1} r\left[\overline{\omega_\theta(\rho u_z^2 + P)} - \rho\overline{u_z u_\theta \omega}_z - \overline{P\frac{\partial u_r}{\partial z}}\right]\mathrm{d}S. \tag{11.100}$$

On the other hand, applying (11.45) along with (11.47) to the open surface of the blade, after neglecting the viscous stresses we obtain

$$M_z = -\frac{1}{2}\int_{S_\mathrm{b}}\rho r^2\sigma_{pz}\,\mathrm{d}S + \frac{1}{2}\oint_{\partial S_\mathrm{b}} pr^2\,\mathrm{d}z, \tag{11.101}$$

where $S_\mathrm{b}$ is the area of the blade surface with $\partial S_\mathrm{b}$ being its boundary line at the juncture with the hub. Therefore, a simultaneous analysis of the integrand of $\beta$, $\eta$, and $\boldsymbol{M}$ forms a basis of local-dynamics diagnosis and can fill the gap between conventional analysis and blade design. the extension to compressible flow is straightforward.

Li and Guo (2005) have applied (11.99) and (11.100) to diagnose the blade design of a test model of low-speed compressor. Under the design condition, the rotational speed is 3000 rpm, total-pressure ratio was 150 mm (water),

total mass flux was $2.4\,\mathrm{m}^3\,\mathrm{s}^{-1}$, and efficiency was 85%. They found that the dominant local-dynamics mechanism in both (11.99) and (11.100) is a strong $\omega_\theta > 0$, of which the best favorable effect occurs at large $r$, i.e., near the shroud. By a Reynolds-averaged Navier–Stokes computation, Li and Guo observed a quite uniform distribution of the total-pressure flux $Pu_z$ across a sectional plane at the blade trailing edge, but this performance was deteriorated under small-flux condition and became the worst when stall occurred. The corresponding distributions of $\omega_\theta$ indicated that the efficiency drop is associated with the accumulation of large $\omega_\theta$ toward the region of smaller $r$. Based on this diagnosis and using (11.101), then, Li and Guo conducted a redesign of the blade shape, see Fig. 11.27, which improved significantly the uniformity of the $\omega_\theta$-distribution under the off-design conditions.

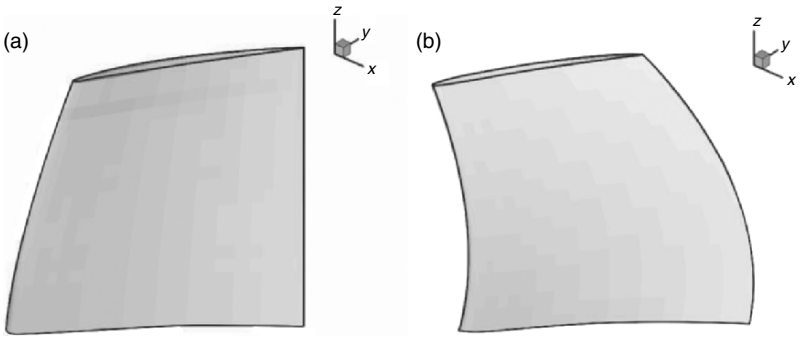


**Fig. 11.27.** (**a**) The original blade shape of a test model of low-speed compressor, and (**b**) the improved shape based on local-dynamics diagnosis. Courtesy of Li

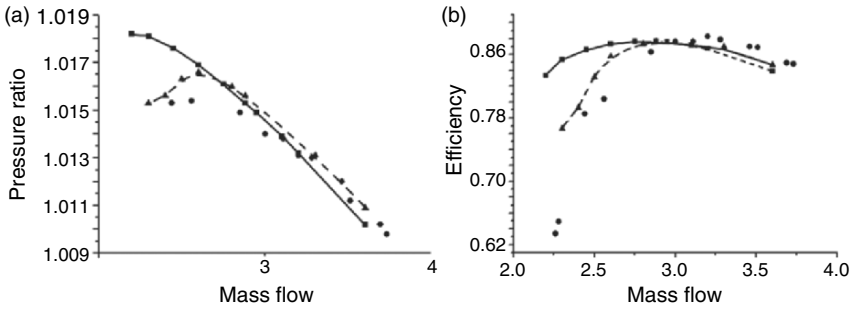


**Fig. 11.28.** The performance of the two blade shapes of Fig. 11.27. (**a**) total pressure ratio. (**b**) Efficiency. *Dashed line* and *solid line* represent the numerical results for the original blade and new blade, respectively. The *filled circles* are the experimental results of the original blade. Reproduced from Li and Guo (2005)

The total-pressure ratio and efficiency were accordingly enhanced at small-flux side, as evidenced by Fig. 11.28. The stall margin is considerably enlarged.

## Summary

1. The emphasis of the aerodynamics theories presented in this chapter is to reveal the local dynamic processes that have net contribution to the total force and moment. This information is very valuable for understanding the physics and in flow diagnosis, configuration design, and flow control. The local dynamic processes are measured by the spatial–temporal derivatives of relevant flow quantities, which at large Reynolds numbers are highly localized to a few discrete peaks associated with key flow structures. These structures have full appearance only in differential equations, but can be made reappear in integrated force and moment by projection or derivative-moment transformations (DMT). Both types of approaches arrive at the same overall physical picture: at low Mach numbers the dominant mechanism in the force and moment is the shearing process, while at supersonic Mach numbers it becomes the compressing process.
2. The projection theory projects the Navier–Stokes equation onto the vector space spanned by the unit acyclic potential velocities and then take integration. In particular, the integrated pressure force is replaced by those terms in the momentum balance that characterize the shearing and compressing processes, mainly the Lamb vector (vortex force) and density variation. The theory applies to externally unbounded fluid at rest at infinity or having uniform velocity. Due to the fast far-field convergence of the acyclic potential velocity, the force can be calculated from the flow data in a sufficiently large but finite domain.
3. The DMT-based theory transforms the integrands of standard force and moment formulas by the moments of their spatial–temporal derivatives that represent the local dynamics. In its general form, the theory is formulated for arbitrary domain, of which the outer boundary can extend to infinity, remain finite, or shrink to the body surface. This flexibility permits a global view, a mid-field view, a near-field view, and an on-wall close view, respectively. At two opposite extremal views, the theory recovers the infinite-domain vorticity-moment theory and boundary vorticity-flux theory, respectively. The former is the first systematic DMT-based theory for the force and moment, with very intuitive vortex-dynamics interpretation. The classic incompressible aerodynamic theories can be easily deduced from these DMT-based theories at certain approximate levels.
4. For the same flow field, each view of the DMT-based arbitrary-domain theory has its own key dynamic mechanism as the net contributor to the total force and moment. These include the rate of change of impulse and angular impulse, the Lamb-vector integrals along with unsteady vorticity moments, the vorticity diffusion moments, and the stress-related

boundary vorticity fluxes, etc. These multiple pictures reflect different evolution stages or aspects of the same flow; capturing any one of them can lead to the correct total force and moment. Therefore, a rich "multi-dimensional" means is available for a thorough flow analysis.

5. High-accuracy estimate of total force by experimentally measured data also calls for unconventional expressions with easily measurable integrand. Vorticity dynamics and DMT help achieve this goal and clarify some long-standing issues. For steady incompressible flow at large Reynolds numbers, the minimum requirement for the measurement is to survey a wake plane over the region where disturbance velocity is nonzero. To survey a small vortical region of the wake plane, one can obtain the profile drag but at most a good yet still approximate estimate of the lift, and a rough estimate of the induced drag. For unsteady incompressible flow, the use of a proper DMT identity permits an accurate estimate of total force by surveying the flow data on a control surface alone.
6. The application of derivative-moment transformations is not confined to external flow problems. The theory may well be applied to local-dynamics diagnosis of internal flows with different performance parameters.